State dependent particle dynamics in liquid alkali metals

2006 J. Phys.: Condens. Matter 18 R585

(http://iopscience.iop.org/0953-8984/18/37/R01)

INSTITUTE OF PHYSICS PUBLISHING JOURNAL OF PHYSICS: CONDENSED MATTER

J. Phys.: Condens. Matter **18** (2006) R585–R633 doi:10.1088/0953-8984/18/37/R01

TOPICAL REVIEW

State dependent particle dynamics in liquid alkali metals

W-C Pilgrim[1,3] **and Chr Morkel**[2]

[1] Department of Chemistry, Physical-Chemistry, Philipps-University of Marburg, D-35032 Marburg, Germany
[2] Physics Department, E21 of the Technical University of Munich, D-85747 Garching, Germany

E-mail: pilgrim@mailer.uni-marburg.de

Received 6 February 2006, in final form 3 July 2006
Published 24 August 2006
Online at stacks.iop.org/JPhysCM/18/R585

Abstract

This paper gives a survey of the particle dynamics in the liquid alkali metals observed with inelastic x-ray and neutron scattering experiments. Liquid rubidium and sodium are chosen as model fluids to represent the behaviour of this group of fluids. In the dense metallic monatomic melt the microscopic dynamics is characterized by collective excitations similar to those in the corresponding solids. The collective particle behaviour is appropriately described using a memory function formalism with two relaxation channels for the density correlation. A similar behaviour is found for the single particle motion where again two relaxation mechanisms are needed to accurately reproduce the experimental findings. Special emphasis is given to the density dependence of the particle dynamics. An interesting issue in liquid metals is the metal to non-metal transition, which is observed if the fluid is sufficiently expanded with increasing temperature and pressure. This causes distinct variations in the interparticle interactions, which feed back onto the motional behaviour. The associated variations in structure and dynamics are reflected in the shape of the scattering laws. The experimentally observed features are discussed and compared with simple models and with the results from computer simulations.

(Some figures in this article are in colour only in the electronic version)

Contents

[3] Author to whom any correspondence should be addressed.

1. Introduction

Since the early studies on diffusion by Robert Brown about 170 years ago, the search for a broad understanding of the particle motion in liquids has attracted numerous scientists worldwide and this type of research is still an extraordinarily challenging task from the theoretical as well as from the experimental point of view. Despite the enormous efforts that have been invested in this field over the last 50 years and the vast number of excellent experimental and theoretical results, we are still far from fully comprehending the collective and single particle motion of atoms and molecules in disordered fluid phases on a microscopic scale and relating it to the bulk properties of a liquid. There is still much that needs to be done.

In order to understand at least the basic concepts of the particle motion in fluid systems, much work was focused on the so called 'simple liquids', which by definition are composed of particles interacting through radial symmetric central forces and which do not comprise internal degrees of freedom. Two prominent examples seem perfectly to obey this classification, the fluid noble gases and the liquid alkali metals, and in fact both have been objects of investigation in numerous scattering experiments, *molecular dynamics* (MD) simulations and also many theoretical approaches over the past five decades. However, except the common classification of being simple, the two systems do not really have much in common. This is already apparent from the different thermophysical properties, e.g. the temperature/pressure ranges where the liquids coexist with their vapour phases. The normal pressure melting points of the noble gases—if available at all—range from about 25 K for neon up to 161 K for xenon, and in all cases the liquid–vapour coexistence curves extend only over a few degrees. In contrast, the melting temperatures of the alkalis extend from room temperature conditions for caesium (29 °C) to about 181 °C for lithium, and they all comprise very wide liquid–vapour coexistence ranges with high critical temperatures (see [1]). The microscopic properties in both systems also significantly differ. It is now a well established fact that the dynamics in molten alkali metals is strongly influenced by distinct collective modes, which extend down to wavelengths comparable to interatomic separations, similar to the phonons in the corresponding crystalline solids. In liquid noble gases, such excitations are only well defined at long wavelength, where they are rather interpreted as classical density fluctuations. Of course, all these characteristic discrepancies have their origin in the specific particle interactions, which are fundamentally different for both systems: in a noble gas, the valence electrons are localized and the interparticle potentials result from dispersion forces, which have their origin in the polarizability of the electron cloud around each atom. This situation leads to the well

known Lennard-Jones pair potentials for the noble gases, which account quite well for the thermophysical properties of the dense liquids as well as for the dilute gas phase:

$$V(r) = 4\varepsilon \left[\left(\frac{r_0}{r} \right)^{12} - \left(\frac{r_0}{r} \right)^{6} \right]. \tag{1.1}$$

ε and r_0 are characteristic constants specific for each element of this group; they determine the depth of the potential well and the position of the first zero in $V(r)$, respectively. The Lennard-Jones potentials are real pair potentials. This means that the influence of a third particle on the polarization induced between a certain pair of atoms remains small even in a dense liquid. Hence, the total potential energy of the system can always be expressed as a sum of pair interactions and equation (1.1) is valid at all densities. In fact, a common procedure for liquid state theory is to determine the parameters in equation (1.1) using measured properties from the gas phase.

The situation is completely different for the liquid alkali metals, where each atom contributes one single electron to a delocalized electron gas. Such a system is better described as an arrangement of positively charged ions embedded into a negatively charged electronic background. In the common approach the interparticle interactions are constructed from Coulombic forces, screened by the negative charge distribution of the conduction electrons. Hence, the potentials between the particles in a metal rather result from the collective behaviour of the electrons and ions than from simple two particle correlations. This already makes it clear that the term 'simple liquid' is a crude oversimplification for the fluid alkali metals. Additionally, in contrast to the non-conducting liquid noble gases where equation (1.1) describes the particle interaction along the whole range of the liquid state, for a metal no such potential can exist which is valid along the full liquid density range. No matter how the potential energy in a metal is formulated, one always has to take into account the influence of the electron gas on the ionic cores. Therefore, such a description must always be a function of the electron density and hence of the metal density itself. In order to maintain the concept of *pairwise* interactions also in liquid metals *pseudo-potential theory* was 'invented', which allows the computation of the so-called *effective pair potentials*. They take into account a specific empty core interaction for the bare ions screened by the surrounding electron density. Several useful effective pair potentials have been suggested over the last 30 years. One of the most prominent, which has widely found application, is the so called Price potential [2]:

$$V(r) = \frac{(Ze)^2}{r} \left[1 - \frac{2}{\pi} \int_0^\infty G(Q) \frac{\sin(Qr)}{Qr} \, \mathrm{d}Q \right]. \tag{1.2}$$

Here, Z defines the ionic charge and $G(Q)$ is a function containing the Fourier transform of the Ashcroft empty core pseudopotential [3] together with a modified Q-dependent dielectric function [4]. The latter depends on density through the Fermi wavevector k_F. This potential was shown to reproduce the thermophysical properties of dense liquid sodium remarkably well. Also, structural and dynamical features of the liquid alkali metals were calculated and a reasonable agreement with MD data [5] was found. For argon and sodium, which both belong to the same row in the periodic table, the respective pair potentials obtained from equations (1.1) and (1.2) are compared in figure 1.

The differences between the potentials are apparent: the well depth is considerably larger for the metal, and while the Lennard-Jones potential asymptotically returns to zero the Price potential shows an oscillatory behaviour with increasing r. These are the so called Friedel oscillations, which formally originate from a discontinuity of the dielectric function at $2k_\mathrm{F}$. It also turns out that the repulsive part of the Lennard-Jones interaction is considerably steeper than for the metal (see the inset in figure 1). The latter has an important influence on the

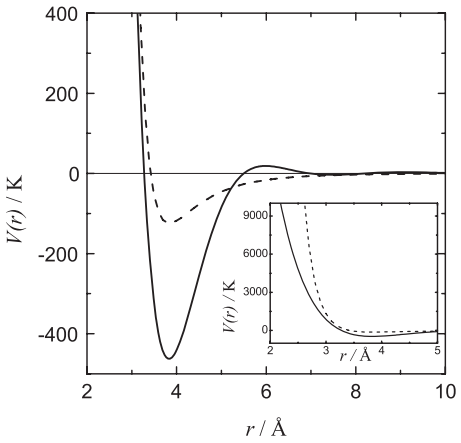

Figure 1. Pair potentials for argon (dashed line) and sodium at 373 K (solid line) obtained from equations (1.1) and (1.2). In the inset the energy scale is extended to higher values to demonstrate the difference in the repulsive contribution.

microscopic collective motion of the particles as was recently demonstrated by a series of MD simulations on corresponding model systems [6].

Since potentials like (1.2) contain the density dependent variable k_F they may in fact be applicable along a limited density range for which the assumption of a free electron gas, necessary to account for the screening, holds. However, they can never cover the full density range of the liquid metal, which extends from melting point conditions up to the liquid–vapour critical point. At sufficiently reduced densities the screening of the ionic Coulomb potentials breaks down and the electrons start to localize, i.e. a metal to insulator transition sets in. For the liquid alkali metals this occurs if the density is reduced to about three to two times the critical density ρ_{crit} [1, 7].

When the electrons localize, the resulting ns^1-electronic configuration of the neutral alkali atoms favours the formation of molecular aggregates, and in fact dimer–monomer equilibria are well known from the dilute vapour, where all electrons are localized and the alkalis are clearly insulating. Molecular aggregates may therefore be expected if electron localization in the liquid can no longer be suppressed, say, below $3\rho_{crit}$. The investigation of the metal to non-metal transition and its associated features is not possible employing conventional MD simulations, since potentials like the one in equation (1.2) are not able to cope with the localization of the conduction electrons. Hence, the failure of these methods to accurately reproduce the dynamical properties in this temperature/density range is not unexpected. However, the electron localization and also the subsequent formation of molecule-like aggregates can be simulated employing modern *ab initio* methods [8–10] and in fact the results obtained from such calculations are in very good agreement with the experimental observations.

Since the metal to non-metal transition in liquid alkali metals is associated with such high temperatures that thermal ionization must also be taken into account, complicated thermal equilibria between atomic ions, electrons, neutral atoms, molecular structures and their corresponding charged counterparts are expected to control structure and dynamics of such a fluid. Regarding the hot fluid as a weakly ionized plasma, the density dependent concentrations of these species can in principle be calculated using standard methods of chemical thermodynamics and statistical mechanics. For fluid caesium such calculations were carried out [11]; the result is shown in figure 2. It turns out that below about twice the critical

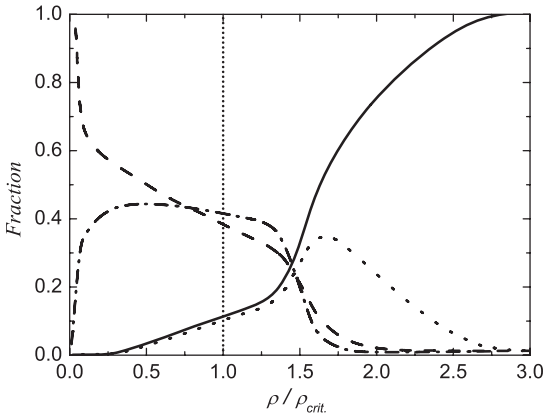

Figure 2. Relative fraction of species in hot low density fluid caesium. The solid line gives the density dependence of the free electron concentration, the dash–dotted line that of Cs dimers, the dotted line Cs_2^+ and the dashed line neutral Cs atoms. Critical density at $\rho/\rho_{\rm crit} = 1$ (vertical dotted line).

density the hot fluid is in fact a mixture of ionized and neutral atoms, dimers, charged dimers and freely moving electrons.

Apparently, depending on density the liquid alkali metals show a diverse variety of interesting features: at high densities the liquid comprises a unique solid-like behaviour characterized by distinct collective motions on a microscopic scale, while at sufficiently reduced particle density, driven by electron localization, intrinsic chemical variations occur which considerably influence the atomic and molecular structure of these systems. We therefore regard it as a scientific challenge of the first order to seek for a microscopic understanding of the characteristic changes that take place during the continuous expansion of a liquid alkali metal, and from the experimental point of view inelastic scattering experiments appear to be ideally suited for this task.

In this review we are discussing the characteristic changes in the particle motion which are observed if a liquid alkali metal is expanded with increasing temperature and pressure. The considered density range extends from melting point conditions up to the low density region in the vicinity of the liquid vapour critical point. The experimental data we are referring to have been obtained from inelastic neutron- and x-ray scattering experiments on liquid sodium and on liquid rubidium. Although data are only presented for these two metals, we think that the observed properties and the conclusions that are drawn from the data analysis also hold for the other members of this group. The general ability to scale the physical properties of liquid alkali metals has been widely demonstrated in the past. E.g., Hensel and co-workers have shown that the thermophysical properties of the alkali metals seem perfectly to obey the so called law of corresponding states, i.e. the phase diagrams from sodium to caesium coincide if appropriately scaled (see [1, 14] and references therein). Also, the structure factors for Na, K, Rb and Cs coincide after suitable scaling [12]. Only the inclusion of lithium seems to be a problem [13] although the features of the dynamic scattering law appear to be identical to those of other alkali metals [27, 62, 63]. The same scalability is found for the dynamic properties of Na, K, Rb and Cs as obtained from computer simulations, where it is also shown that experimental data on Cs scaled in the same way do also coincide on the calculated curves [80]. Hence, we suppose that the dynamic microscopic features can as well be scaled and that properties found in liquid sodium and rubidium are indeed characteristic for the other liquid alkalis, although differences from liquid lithium might exist.

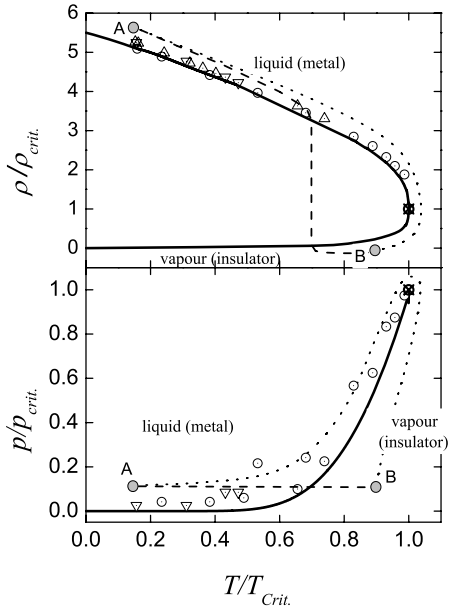

Figure 3. Schematic representation of a liquid/vapour phase diagram for an alkali metal in the p–T- and ρ–T-planes. p, T and ρ are normalized to critical values. Triangles show INS and IXS experiments on liquid Na; circles represent INS experiments on liquid Rb. Dashed line AB corresponds to a temperature rise at constant pressure, i.e. the conventional evaporation procedure. Solid line, coexistence curve; dotted line, possible path to expand a liquid continuously without inducing a liquid–vapour phase transition.

2. Experimental aspects

2.1. Sample handling

The liquid state extends over wide density ranges from melting point conditions up to the liquid–vapour critical point. For a comprehensive understanding and characterization of a specific liquid it is therefore essential to extend any investigations along this entire range if this is experimentally feasible. The ability to vary the liquid density continuously from melting towards the low density regime close to the liquid–vapour critical point is hence an absolutely indispensable requirement. This can only be accomplished if temperature and pressure of the sample are simultaneously varied, e.g. along the liquid vapour coexistence curve to avoid evaporation. This is indicated in figure 3 by the dotted line. The figure shows two ways to transfer a liquid into the vapour phase. The dashed line from A to B corresponds to the normal evaporation process at constant pressure while along the dotted line p and T are simultaneously varied and the liquid continuously transforms into the gaseous state without crossing the vapour pressure curve (solid line), i.e. the two phase region of the system. Also given in the figure are some p–T-points representing the conditions where the scattering experiments were carried out which are reported in this review. To access the low density regime of a liquid, conditions close to the liquid–vapour critical point (CP) need to be approached. Unfortunately, in the case of the liquid alkali metals the critical points lie at extremely high temperatures and also at elevated pressures, conditions which are difficult to realize experimentally (see corresponding values in table 1).

Table 1. Critical temperatures and critical pressures of the liquid alkali metals [14]. Values for Li are taken from [15].

	T_{crit} (K)	p_{crit} (bar)	ρ_{crit} (g cm^{-3})
Li	∼3500	∼380	∼0.11
Na	2485	244	0.175
K	2178	146	0.17
Rb	2017	122.8	0.29
Cs	1924	91.3	0.38

Many experimental efforts were undertaken over the past 40 years to cope with the extreme conditions of temperature and pressure and also with the extremely corrosive nature of the molten metals. A large number of experiments were carried out, e.g. measurements of the equation of state data, the electrical and magnetic properties and also scattering experiments to determine the characteristic variations in microscopic structure associated with the expansion of the metals (for an excellent review see [1] and references therein). More recently, these techniques were appropriately modified to be also applicable in inelastic scattering experiments [16, 17]. Despite the progress in the development of high temperature and high pressure sample environments for neutron and x-ray scattering, it must be kept in mind that such experiments are still extremely sophisticated and a lot of experience is needed to successfully perform these investigations.

2.2. Experimental techniques

An increased interest in particle dynamics in disordered systems could be observed over the past few years. Responsible for this renewed attention are mainly two technological developments: one important impulse came from the recent rapid increase in computer speed which allowed the MD simulations to be carried out with realistic particle numbers over sufficiently long timescales to comprehensively explore the microscopic motion. The big advantage of these 'computer experiments' is that even those dynamical functions that cannot usually be accessed in real experiments are available. Also, pair potentials can be tested from comparing structural and dynamical properties of the computer generated model systems with real experimental data.

The second advancement is purely experimental and related to the advent of the third generation synchrotrons over the last ten years, through which a large number of ingenious x-ray techniques became available. Among them and of fundamental importance for the field of liquid dynamics was the development of high resolution inelastic x-ray scattering (IXS). The basic concepts of this technique have already been outlined many years ago [18, 19]; however, the simultaneous requirement of high resolution and sufficiently high flux has hampered this method for a long time. Over the last decade, many technical difficulties were solved, partly due to the new synchrotrons but also due to technical and material related improvements of those components needed for high resolution energy discrimination of the x-rays [20–23]. Although inelastic neutron scattering (INS) is still the most used technique to study liquid dynamics and in many aspects it may still be superior over x-rays, the new technique comprises specific advantages compared to neutrons which makes it perfectly suited for the investigation of the collective dynamics in condensed matter. Firstly, the scattered radiation is purely coherent over the energy range where particle dynamics is studied. In neutron scattering, many nuclei contribute a considerable incoherent intensity, which often dominates the scattering law and hinders accurate measurements of the collective dynamics. E.g., for liquid sodium it has never been possible to sufficiently separate the incoherent scattering from the neutron data to obtain

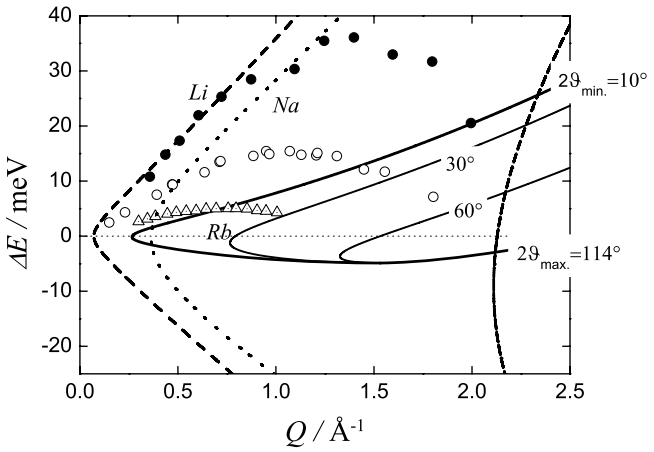

Figure 4. Available Q–ΔE-range for different time of flight spectrometers (all at the ILL), where ΔE determines the energy transfer. IN6 (full lines), IN4 (dotted line) and BRISP (dashed lines). Also shown are dispersion relations of the collective excitations in Li (●), Na (○) and Rb (△). Angles on the right-hand side of the figure determine minimum and maximum angles available at the IN6 instrument.

the purely coherent dynamic scattering law $S(Q, \omega)$ [24–26] as both contributions are of the same order.

Secondly, and perhaps even more important, is the fact that $S(Q, \omega)$ measured with IXS is not hampered by any kinematical restrictions: in an inelastic scattering experiment the dependence of the measured momentum transfer $\vec{Q} = \vec{k}_\mathrm{f} - \vec{k}_\mathrm{i}$ on the scattering angle 2ϑ is given by

$$Q^2(2\vartheta, \vec{k}_\mathrm{i}) = k_\mathrm{f}^2 + k_\mathrm{i}^2 - 2k_\mathrm{f}k_\mathrm{i}\cos(2\vartheta), \tag{2.1}$$

where $\vec{k}_\mathrm{i}$ is the initial momentum of the probe and $\vec{k}_\mathrm{f}$ is the momentum after the scattering event. Inserting the energy–momentum relation for the neutron or the photon into equation (2.1) along with the experiment specific parameters (incident energy and scattering angles) yields the kinematic plane for a particular experiment. For thermal neutrons the incident energy is always of the order of the energy transfer, hence $|k_\mathrm{f}|$ and $|k_\mathrm{i}|$ may noticeably differ. In this case the available part of the kinematic plane restricts the access of larger energy transfers considerably, especially at lower Q. Figure 4 illustrates this situation. There, as an example, the kinematic plane of the time of flight spectrometer IN6 at the ILL in Grenoble, one of the most famous instruments worldwide, is shown for the largest incoming neutron energy available there (4.88 meV). It is confined by the minimum and maximum scattering angles of 10° and 114°. The Q–ΔE-variation at constant angle is exemplarily shown by two paths at 30° and 60°, respectively, where ΔE gives the energy transfer of the scattered neutron in meV. Also depicted are the Q–ω-positions of the collective longitudinal excitations for liquid lithium [27], sodium [28] and rubidium [29]. It is apparent that they are hardly accessible with this spectrometer, especially in the lower momentum transfer region, where the energy of the phonon-like modes increases monotonically with rising Q and where they are well defined.

The rise of the excitation energy in the lower Q-region is approximately determined by the bulk sound velocity in the sample (see section 4.2). Since the slopes of the dispersion relations (symbols in figure 4) give the corresponding phase velocity, this part of the dispersion relation can only be measured if the speed of the incoming neutron is larger than the sound velocity in the sample.

Table 2. Available monochromator settings at the new small angle time of flight spectrometer BRISP.

Monochromator crystal	E_0	λ_0
PG(004)[a]	80.3	1.009
Cu(111)	51.9	1.255
PG(002)[a]	20.1	2.018
Cu(220)	138.3	0.769
Cu(200)	69.2	1.087

[a] PG: highly oriented pyrolytic graphite.

To improve the kinematic situation, higher incoming neutron velocities are needed, which, however, hampers the resolution, and generally shifts the accessible momentum transfer range to higher Q. Therefore, it is also necessary to reduce the minimum scattering angle. The dotted line in figure 4 represents the Q–ω-path of the $2\vartheta = 3°$ angle-spectrum of the IN4 spectrometer of the ILL, which can be operated with an incoming energy of 100 meV. Still the Na-dispersion relation is only partly available and data for Li are still out of reach. There exist current efforts to improve the situation in developing the new Brillouin spectrometer BRISP at the ILL in Grenoble [30]. This spectrometer is particularly designed to measure wider energy ranges in the lower Q-region. From the technical viewpoint, it combines time of flight techniques of high energy neutrons with small angle capabilities. It represents hence a perfect opportunity for Brillouin investigations but also for other studies where an extended kinematic plane at lower Q is needed, e.g. measurements of the incoherent contribution or dynamic magnetic form factors. The instrument is capable of being operated at an incoming energy of 138.3 meV with a minimum scattering angle of 0.5°. The kinematic plane for this setting is also shown in figure 4. The energy resolution is expected to be 2.5–7.0% of the incoming neutron energy. Some information about the possible monochromator settings on BRISP is given in table 2.

The situation at pulsed neutron sources like ISIS is somewhat different. There, two types of inelastic neutron spectrometers exist, those where a characteristic neutron wavelength can be chosen out of the white neutron pulse and which hence work similarly to the spectrometers at a conventional neutron source and those where the incoming beam contains the full spectrum of the pulse and where monochromatization is carried out before the scattered neutrons reach the actual analyser. The latter situation leads to an inverted representation of the scattering process in vector space, therefore these instruments are called *inverted time of flight spectrometers*. However, the energies that are sorted out for acquisition are in the same range as the incoming energies at conventional spectrometers at neutron reactors. Hence the main difference from the kinematic planes of conventional TOF spectrometers is that the Q–ω-areas are mirror inverted with respect to the energy scale but the access to a wider ω-range, especially at lower Q, is limited in the same way. An example of such an instrument is the TOF spectrometer IRIS at the ISIS neutron facility in the UK [31]. More interesting with respect to an expansion of the kinematic plane is the other group of spectrometers at pulsed neutron sources working with a monochromatized incoming radiation, for example the MARI spectrometer also operating at the ISIS facility [32]. Due to the broad energy distributions of the neutron pulse, neutron energies as high as 1000 meV can be sorted out, leading to a considerable widening of the kinematic plane and hence to an access of larger frequencies at lower Q. However, as already mentioned above, this gain in Q–ω-space is paid for by a considerable deterioration of the energy resolution.

For x-rays the situation is completely different: although the incoming energy of the photon is restricted to the few backscattering reflections of the monochromator crystal, the

energy of the incoming photon is always very much larger than the interesting energy transfer range (e.g. 17.9 keV for the Si (9 9 9) reflection at the ID-16 [33] of the ESRF in Grenoble compared with at most ∼100 meV for ΔE). Hence, the condition $|k_f| \approx |k_i|$ is always fulfilled and equation (2.1) reduces to

$$Q \approx 2k_i \sin\vartheta, \tag{2.2}$$

i.e., the momentum transfer solely depends on the scattering angle. IXS measurements are therefore naturally carried out at constant Q and the available energy range is virtually not limited by the momentum transfer. Additionally, since the beam size is considerably smaller than in a neutron experiment, angles less than 1° can easily be obtained, which generally allows the measurement of wide energy transfer ranges even at low Q-values, and in principle all of the dispersion relations shown in figure 4 can be accessed. These advantageous properties of IXS made possible the measurement of the dynamic scattering laws for a variety of liquid systems over the last 10 years which were either not at all attainable before or at least not with such high quality.

3. Theoretical basics

Subsequently, a short survey is given of the basic theoretical background needed to discuss the data presented in the following sections. This section is not intended to give a comprehensive review of theoretical concepts in liquid dynamics but rather to summarize the basic theoretical tools indispensable for the experimentalist to analyse inelastic scattering data of liquid systems. For the reader who is interested in a deeper approach a large number of excellent monographs (see e.g. [34–37]) and recent reviews (e.g. [38, 39]) exists which are more detailed and may also be more lucidly written. Here, we will additionally concentrate solely on a classical view, since the presented data are not discussed within the context of quantum effects.

The measured quantity in an inelastic scattering experiment is the double differential cross section which gives the number of particles (neutrons or x-ray photons) which per unit time are scattered into unit area $r^2 d\Omega$ and energy interval $d\omega$. For x-ray and neutron scattering the double differential cross sections take the following forms [40, 41]:

$$\begin{aligned} &\text{(Neutrons)} \qquad \frac{\partial^2\sigma}{\partial\Omega\partial\omega} = \frac{k_f}{k_i} b^2 S(Q,\omega) \\ &\text{(x-rays)} \qquad \frac{\partial^2\sigma}{\partial\Omega\partial\omega} = \frac{k_f}{k_i} (\vec{e}_i \cdot \vec{e}_f)^2 r_e^2 |f(Q)|^2 S(Q,\omega), \end{aligned} \tag{3.1}$$

where b is the neutron scattering length of the nucleus under investigation, r_e^2 is the Thomson cross section of the electron $\cdot$ (7.95×10^{-26} cm^2) and $f(Q)$ denotes the atomic form factor. k_i and k_f represent the modulus of the probe momentum before and after the scattering event (note that $k_f/k_i \approx 1$ for x-rays) and $\vec{e}_i$ and $\vec{e}_f$ give the direction of the electric field vector for the x-radiation before and after scattering.

For neutrons, the scattering length b of the nuclei in a sample may statistically vary from site to site due to the presence of different isotopes and/or different nuclear spin states. Since the spins and different isotopes are not correlated, averaging of the scattering length leads to an additional scattering contribution which does not show any phase correlation. This additional intensity is accounted for by the incoherent neutron scattering cross section. Hence we have generally two contributions to the scattering law obtained from neutron scattering which are

defined by

$$\left(\frac{\partial^2\sigma}{\partial\Omega\partial\omega}\right)_{\text{coh}} = \frac{k_\text{f}}{k_\text{i}}\,\langle b\rangle^2\,S(\vec{Q},\omega) \qquad \text{and}$$
$$\left(\frac{\partial^2\sigma}{\partial\Omega\partial\omega}\right)_{\text{incoh}} = \frac{k_\text{f}}{k_\text{i}}\left(\langle b^2\rangle - \langle b\rangle^2\right)S_{\text{incoh}}(\vec{Q},\omega). \tag{3.2}$$

The brackets $\langle\cdots\rangle$ in equation (3.2) and in subsequent expressions symbolize an ensemble average. $S(Q,\omega)$ and $S_{\text{incoh}}(Q,\omega)$ represent the coherent and incoherent scattering laws, respectively. One immediately sees that the incoherent contribution vanishes if there is no fluctuation among the scattering lengths. Both functions are exclusively determined by the properties of the sample and scattering theory yields [34]

$$S(\vec{Q},\omega) = \frac{1}{2\pi N}\int_{-\infty}^{+\infty}\mathrm{d}t\,\mathrm{e}^{-\mathrm{i}\omega t}\sum_{j,k}^{N}\left\langle \mathrm{e}^{-\mathrm{i}\vec{Q}\cdot\vec{r}_j(0)}\mathrm{e}^{-\mathrm{i}\vec{Q}\cdot\vec{r}_k(t)}\right\rangle \qquad \text{and}$$
$$S(\vec{Q},\omega) = \frac{1}{2\pi N}\int_{-\infty}^{+\infty}\mathrm{d}t\,\mathrm{e}^{-\mathrm{i}\omega t}\sum_{j=1}^{N}\left\langle \mathrm{e}^{-\mathrm{i}\vec{Q}\cdot\vec{r}_j(0)}\mathrm{e}^{-\mathrm{i}\vec{Q}\cdot\vec{r}_j(t)}\right\rangle. \tag{3.3}$$

The meaning of equation (3.3) is that we could immediately calculate the scattering law if we *a priori* knew the positions of all the particles in our sample at all times or equivalently the corresponding ensemble averages. Equations (3.3) therefore represent the link between a theoretical approach to the particle motion and the outcome of a real experiment.

The route to a general description of the microscopic particle motion was firstly outlined by the famous work of Leon van Hove [42] in defining the fundamental function $G(\vec{r},t)$, the space–time correlation function as the Fourier transform of the scattering law $S(\vec{Q},\omega)$. It is a measure of the correlation between the microscopic local density at time t and coordinate r with the local density at another time and another point in space. This function reads

$$G(\vec{r},t) = \frac{1}{N}\left\langle n_\text{i}(\vec{r}=0,t=0)\cdot n_j(\vec{r},t)\right\rangle, \tag{3.4}$$

where $n(\vec{r},t)$ stands for the local particle density and is given by the useful definition

$$n_j(\vec{r},t) = \sum_{j=1}^{N}\delta(\vec{r}-\vec{r}_j(t)). \tag{3.5}$$

The function defined in equation (3.4) is called the van Hove space–time correlation function and is related to the scattering law by a double Fourier transform in space and time:

$$S(\vec{Q},\omega) = \frac{1}{2\pi}\int_{-\infty}^{+\infty}\int_{-\infty}^{+\infty}\mathrm{e}^{\mathrm{i}(\vec{Q}\cdot\vec{r}-\omega t)}G(\vec{r},t)\,\mathrm{d}\vec{r}\,\mathrm{d}t. \tag{3.6}$$

Accordingly, a function $G_{\text{self}}(\vec{r},t)$ is defined as the Fourier transform of the incoherent scattering law:

$$S_{\text{incoh}}(\vec{Q},\omega) = \frac{1}{2\pi}\int_{-\infty}^{+\infty}\int_{-\infty}^{+\infty}\mathrm{e}^{\mathrm{i}(\vec{Q}\cdot\vec{r}-\omega t)}G_{\text{self}}(\vec{r},t)\,\mathrm{d}\vec{r}\,\mathrm{d}t. \tag{3.7}$$

Consequently, this function gives the probability of finding a tagged particle at time t and position r; if at $t=0$ it has been at $r=0$, it reads

$$G_{\text{self}}(\vec{r},t) = \frac{1}{N}\left\langle n_\text{i}(\vec{r}=0,t=0)\cdot n_\text{i}(\vec{r},t)\right\rangle, \tag{3.8}$$

with $n_\text{i}(\vec{r},t)$ being the single particle local density

$$n_\text{i}(\vec{r},t) = \delta(\vec{r}-\vec{r}_\text{i}(t)). \tag{3.9}$$

From equations (3.1) to (3.9), a number of relations can be derived which play an important role in the interpretation of inelastic scattering data, but not all of them are really attainable from experiment.

Spatial Fourier transformation of equation (3.4) gives the so called coherent intermediate scattering function $F(Q,t)$:

$$F(\vec{Q},t) = \frac{1}{N}\left\langle n_Q^*(0)\cdot n_Q(t)\right\rangle. \tag{3.10}$$

Now, the $n_i(\vec{r},t)$ have turned into the Fourier components $n_Q(t)$ of the local densities (the subscripts i and j are from now on omitted for clarity). They are often interpreted as plane waves and may be interpreted as density fluctuations with wavevector Q:

$$n_Q(t) = \sum_{j=1}^{N} \exp\left\{\mathrm{i}\vec{Q}\cdot\vec{r}_j(t)\right\}. \tag{3.11}$$

The intermediate scattering function is perhaps the most central quantity in the theoretical framework of liquid dynamics. It is therefore sensible to consider this quantity in some more detail: evidently, from its definition, $F(\vec{Q},t)$ is related to the scattering law by a Fourier transform in time,

$$F(\vec{Q},t) = \frac{1}{\sqrt{2\pi}}\int_{-\infty}^{+\infty} \mathrm{e}^{\mathrm{i}\omega t} S(\vec{Q},\omega)\,\mathrm{d}\omega. \tag{3.12}$$

At short times we may formally approximate the shape of $F(\vec{Q},t)$ from a Taylor expansion,

$$F(\vec{Q},t) = F(\vec{Q},0) + \left.\dot{F}(\vec{Q},t)\right|_{t=0}\cdot t + \left.\ddot{F}(\vec{Q},t)\right|_{t=0}\cdot\frac{t^2}{2} + \cdots, \tag{3.13}$$

where the coefficients are given through the time derivatives of (3.12):

$$\begin{aligned}
F(\vec{Q},0) &= \frac{1}{\sqrt{2\pi}}\int_{-\infty}^{+\infty} S(\vec{Q},\omega)\,\mathrm{d}\omega \equiv \left\langle\omega^0\right\rangle = S(\vec{Q})\\
\left.\dot{F}(\vec{Q},t)\right|_{t=0} &= \mathrm{i}\frac{1}{\sqrt{2\pi}}\int_{-\infty}^{+\infty} \omega S(\vec{Q},\omega)\mathrm{d}\omega \equiv \left\langle\omega^1\right\rangle = 0\\
\left.\ddot{F}(\vec{Q},t)\right|_{t=0} &= -\frac{1}{\sqrt{2\pi}}\int_{-\infty}^{+\infty} \omega^2 S(\vec{Q},\omega)\,\mathrm{d}\omega \equiv \left\langle\omega^2\right\rangle\\
\left.\dddot{F}(\vec{Q},t)\right|_{t=0} &= \cdots.
\end{aligned} \tag{3.14}$$

From (3.14) we recognize that the expansion coefficients in equation (3.13) are identical to the nth order frequency moments $\langle\omega^n\rangle$ of the scattering law. Since in the classical limit $S(Q,\omega)$ is a symmetric function centred at $\omega = 0$, all the odd moments are equal to zero. However, the measured $S(\vec{Q},\omega)$, even in the classical limit, is usually not symmetric because at not too high temperature the excitation process in the liquid, observed on the energy loss side of the neutron spectrum, is more likely to occur than the de-excitation process on the energy gain side. This fact has to be taken into account and usually the measured scattering law is symmetrized by introducing a corresponding Boltzmann factor [34]. The remaining moments, however, can be related to microscopic properties of the liquid: e.g., the zero order moment gives the static structure factor $S(Q)$. Further expressions exist up the sixth order [39]. It turns out that it is practical to formulate the moments in a reduced form, since then they represent characteristic frequencies of the liquid as we shall see later. E.g., the reduced second moment is defined as

$$\omega_0^2(\vec{Q}) = \frac{\left\langle\omega^2\right\rangle}{\left\langle\omega^0\right\rangle} = \frac{k_\mathrm{B}T}{M}\frac{Q^2}{S(Q)}, \tag{3.15}$$

where k_B is the Boltzmann constant and M is the particle mass. The fourth reduced moment, however, is more knotty since its calculation requires a detailed knowledge of the interatomic interaction potential $V(r)$ and the pair correlation function $g(r)$:

$$\omega_L^2(\vec{Q}) = \frac{\langle\omega^4\rangle}{\langle\omega^2\rangle} = \frac{3\,k_B T}{M} Q^2 + \Omega_0^2 - \Omega_Q^2, \tag{3.16}$$

with

$$\Omega_0^2 = \frac{4}{3}\frac{n\pi}{M}\int_0^\infty g(r)\left[\frac{d^2}{dr^2}V(r) + \frac{2}{r}\frac{d}{dr}V(r)\right]r^2\,dr \qquad \text{and}$$
$$\Omega_Q^2 = \frac{n}{M}\int_0^\infty g(r)\frac{d^2}{dr^2}V(r)\cos(\vec{Q}\cdot\vec{z})r^2\,dr, \tag{3.17}$$

where n denotes the number density and the coordinate $\vec{z}$ is chosen to be parallel to the direction of $\vec{Q}$. However, equation (3.16) can be considerably simplified for isotropic simple liquids with spatial short range interactions, and as a good approximation for the reduced fourth moment one finds [43]

$$\omega_L^2(\vec{Q}) = \frac{3k_B T}{M} Q^2 + \omega_E^2\left[1 - \frac{3\sin(\vec{Q}\cdot\vec{r}_0)}{\vec{Q}\cdot\vec{r}_0} - \frac{6\cos(\vec{Q}\cdot\vec{r}_0)}{(\vec{Q}\cdot\vec{r}_0)^2} + \frac{6\sin(\vec{Q}\cdot\vec{r}_0)}{(\vec{Q}\cdot\vec{r}_0)^3}\right]. \tag{3.18}$$

Here, ω_E is a characteristic frequency called the Einstein frequency and usually interpreted as the average rattling rate of the atoms in their cage of next neighbours. It is given by

$$\omega_E^2 = \frac{4}{3}\frac{n\pi}{M}\int_0^\infty g(r)\frac{d^2}{dr^2}V(r)r^2\,dr. \tag{3.19}$$

The applicability of the approximation in equation (3.18) was demonstrated by comparing it with reduced fourth frequency moments obtained from computer simulations on Lennard-Jones liquids [44] and on liquid rubidium [45] employing the potentials given in equations (1.1) and (1.2).

The intermediate scattering function can in principle also be obtained from experiment; however, this is a difficult task. Sufficiently high energy resolution is required which on the other hand—depending on momentum transfer—may lead to restrictions in the kinematic plane which also hampers a numerical transformation of the data. Also, in order to obtain a reliable result data with high statistical quality are needed where any scattering background has carefully been removed. Most of the attempts to transform neutron spectra were performed on incoherent scatterers to obtain the incoherent intermediate scattering function, since the incoherent scattering law has a considerably simpler shape. A direct access to $F(\vec{Q}, t)$ is however possible in *neutron spin echo* experiments [46], where, however, the accessible Q–ω-range is very much limited. However, a quantity closely related to the density correlation is the correlation function of the particle currents. From equation (3.11) we can define the Fourier components of the local particle current $\vec{j}(\vec{r}, t)$ as

$$j_Q(t) = \sum_{j=1}^{N} v_j(t)\,\exp\left\{i\vec{Q}\cdot\vec{r}_j(t)\right\} = \frac{1}{iQ}\dot{n}_Q(t), \tag{3.20}$$

where v_j is the velocity of particle j at time t. Actually, equation (3.20) must be split into two transverse and one longitudinal components. Only the longitudinal modes are correlated to the density fluctuations in the system. Since neutrons and x-rays are coupling to the spatiotemporal fluctuations of the density it is the longitudinal collective dynamics which leaves its fingerprint on the scattering law. Therefore, we will deal only with the longitudinal part and hence we have chosen $\vec{z}$ to be identical to the direction of $\vec{Q}$. Naturally, in a dense fluid with highly

correlated local densities the particle flow is expected to be highly correlated as well and we can accordingly define a current–current correlation function $J_L(\vec{Q}, t)$:

$$J_L(\vec{Q}, t) = \frac{1}{N} \left\langle j_{\vec{Q}}^z(0) \cdot j_{\vec{Q}}^z(t) \right\rangle \tag{3.21}$$

(for simplicity the suffix 'z' for the component of the current will from now on be neglected). The Fourier transform of equation (3.21) gives $J_L(\vec{Q}, \omega)$ and it is easily shown that the relation

$$J_L(\vec{Q}, \omega) = \frac{\omega^2}{Q^2} S(\vec{Q}, \omega), \tag{3.22}$$

is valid [35, 36], which allows the direct determination of the current–current correlation function from the measured scattering law. However, although equation (3.22) defines a new correlation function it should be noted that it introduces no further new physics. The advantage of $J_L(\vec{Q}, \omega)$ over the original scattering law is purely experimental as we shall see later.

So far we have performed a purely phenomenological approach to liquid dynamics and as a result we have defined some important correlation functions and the frequency moments of the scattering law. However, from equations (3.1) to (3.22) we do not gain any insight into the microscopic space–time behaviour of the liquid particles. For an understanding of the particle motion on microscopic time- and length-scales we need to invoke microscopic theories which allow the scattering law $S(\vec{Q}, \omega)$ to be modelled for a comparison with experimental results. Some of these models will be presented in the next chapters where their applicability to measured data is also examined. Since we are only dealing with isotropic fluids here, the direction of the measured momentum transfer is of no importance. Hence, in order to keep the formulae clearer we will omit the vector arrow from now on for Q-dependent functions.

4. Collective dynamics

4.1. The hydrodynamic limit

At high density, close to melting, the microscopic dynamics in a liquid comprises a distinct collective character. Fluctuating density–density correlations give rise to transverse and longitudinal phonon-like modes similarly as in a crystalline solid. However, while in the latter case they result from coupled harmonic vibrations of the atoms in an ordered lattice, in liquids they are the consequence of fundamental thermodynamic fluctuations and are better characterized as propagating sound modes. In crystals and in liquids these excitations can be measured using inelastic scattering techniques, where they appear as sidepeaks in the scattering law. This allows investigation of the interesting question of down to what length scales a liquid is capable of sustaining sound modes and how their characteristic properties vary with decreasing wavelength.

In the long wavelength limit (at very low Q), where $S(Q, \omega)$ can be accessed by inelastic light scattering techniques, the measured scattering spectrum from a simple liquid can excellently be described by a sum of three Lorentzians, the so called *Rayleigh–Brillouin triplet*. The underlying physical picture was already unravelled about 40 years ago by Mountain [47] and by Kardanov and Martin [48] in the framework of classical hydrodynamics. Starting from the conservation laws for mass, momentum and energy it was shown that in the case of a simple liquid the experimentally observed pattern can be approximated by three Lorentzian peaks, one located at the centre of the spectrum and the other two at positive and negative energy transfer, respectively:

$$S(Q, \omega) = \frac{S(Q)}{2\pi} \left[\frac{\gamma - 1}{\gamma} \frac{2 D_T Q^2}{\omega^2 + (D_T Q^2)^2} + \frac{1}{\gamma} \frac{\Gamma Q^2}{(\omega \pm Q c_S)^2 + (\Gamma Q^2)} \right]. \tag{4.1}$$

From the thermodynamic viewpoint, the sidepeaks—or Brillouin lines—originate from pressure fluctuations at constant entropy which are created or annihilated in the scattering process. They shift to higher frequency with rising momentum transfer, indicating the propagating nature of these excitations. The shift is determined by the adiabatic speed of sound c_S in the liquid. These are the longitudinal sound modes which travel through the liquid with adiabatic sound velocity. The width of the lines is a measure of the mode lifetime and determined by the sound absorption coefficient Γ, which is related to the thermal diffusivity D_T and the longitudinal viscosity ν_L:

$$\Gamma = \tfrac{1}{2}[(\gamma - 1)D_T + V_L]. \tag{4.2}$$

The central line, the so called Rayleigh peak, results from light scattered by local non-propagating density fluctuations. Their lifetime is determined by the thermal diffusivity D_T and theoretically these modes can be understood as entropy fluctuations at constant pressure. All peaks broaden quadratically with increasing Q.

Both types of fluctuations are correlated, which can already be inferred from the observation that the weight of all three lines is determined by the same quantity γ, the ratio of the heat capacities C_P and C_V. This is quantified in the well known Landau–Placzek ratio [49], which links γ directly to the ratio of the integrated intensities I of the Rayleigh and Brillouin peaks:

$$\gamma - 1 = \frac{I_R}{2I_B}. \tag{4.3}$$

According to (4.1) the ratio of the heat capacities plays a crucial role in determining the relative weight of the Brillouin contribution to the spectrum. The more C_P and C_V resemble each other (i.e. $\gamma \approx 1$) the stronger is the weight of the collective excitations. For the liquid alkali metals close to melting one finds $\gamma \approx 1$ and indeed the spectra show a pronounced collective character. From (4.1) to (4.3) a clear picture evolves about the microscopic processes that lead to the characteristic three line pattern observed in this *long wavelength limit*: a scattered photon creates (or annihilates) a longitudinal vibrational mode, which gives rise to the Stokes or anti-Stokes Brillouin lines. The lifetime of this propagating mode is ruled by two possible relaxation channels, the loss of heat determined by the value of the thermal diffusivity D_T and the loss of energy due to viscous relaxation given by the longitudinal viscosity ν_L. These quantities hence determine the width of the resulting excitation peak (equation (4.2)). While the mode travels through the liquid it leaves behind a trace of adiabatically squeezed and dilated volume elements with diameters of the order of half the mode period $2\pi/Q$, i.e. a trace of temperature and density fluctuations which spatially oscillate about their corresponding average values. These fluctuations decay back to equilibrium on a timescale solely determined by the thermal diffusivity. Scattering from these fluctuations gives rise to the quasielastic scattering contribution, i.e. the Rayleigh peak with width $D_T Q^2$.

With decreasing wavelength (i.e. increasing wavevector) the linewidths of all the peaks broaden quadratically, indicating that the lifetime of the underlying excitations rapidly decreases the smaller the length scale which is probed by the scattered photons becomes. Since the excitation frequency of the mode rises only linearly, an interesting situation may occur if at sufficiently large Q the width of the central Rayleigh peak has adequately broadened and the condition $D_T Q^2 = c_S Q$ is fulfilled. In this case the rate at which heat is piled up due to the adiabatic compression from the mode equals the rate at which heat is dissipated due to thermal conduction. The process is hence no longer adiabatic and modes with larger wavenumbers must propagate with isothermal rather than with adiabatic speed of sound, i.e. with c_T rather than with c_S. Using literature data for c_S [50] and for the computation of D_T [51], one finds that for the alkali metals close to melting this *adiabatic to isothermal transition* already sets in at

wavevectors as small as about 10^{-6} Å^{-1}, which means that a large portion of the waves from the ultrasonic sound spectrum traverses the liquid metal already with the isothermal speed of sound. This is at least the situation if the bulk value for D_T is used, containing the electronic as well as the ionic contribution to heat conductivity. However, it is still an ongoing discussion whether only the ionic part should contribute (see e.g. [52]). In this case the adiabatic to isothermal transition should occur at considerably larger Q-values. However, since in the molten alkalis $\gamma \approx 1$, the difference between c_T and c_S is negligible and the problem is of rather academic interest. However, for other liquids with $\gamma > 1$ this might be an interesting and measurable effect.

4.2. Beyond the hydrodynamic limit

Hydrodynamics is applicable as long as the wavelength of the characteristic fluctuations in the sample is considerably larger than the microscopic diameters. In an atomic fluid such as a compressed noble gas or a liquid metal these diameters may be of the order of interatomic distances. The validity of the hydrodynamic range is therefore often characterized by the condition $\sigma \cdot k \ll 1$, where σ is an atomic diameter related to the position of the structure factor maximum, which is located at about $Q_0 = 2\pi/\sigma$, and $\vec{k}$ is the wavevector of the fluctuation, which in a scattering experiment must match the momentum transfer $\vec{Q}$ of the probe in order to be identified. The ideal tools to investigate the hydrodynamic regime and to verify the predictions from classical hydrodynamics are therefore inelastic light scattering techniques [53], where the condition $\sigma \cdot Q \ll 1$ is certainly valid. Classical hydrodynamics predicts that the excitation energy of the collective modes increases linearly in Q and all three lines of the spectrum broaden with Q^2. At sufficiently high momentum transfer the lines are hence expected to have merged into one broad intensity distribution where the collective modes are no longer discernable. However, following the above given characterization, the hydrodynamic relations should no longer apply if the condition $\sigma \cdot Q \approx 1$ is approached, i.e. if fluctuations on the atomic scale are regarded and if the momentum transfer of the probe is in the range where neutron and x-ray scattering techniques are applicable. Then, molecular dynamics effects certainly need to be taken into account, and it is expected that the hydrodynamic behaviour transforms into the molecular dynamics regime. In fact, it is found that distinct sound modes are still observed at Q values characteristic of atomic length scales. This was first demonstrated by the pioneering work of Copley and Rowe on liquid rubidium in the mid-1970s [29]. Some important neutron investigations followed; however, due to the difficulties mentioned above the breakthrough for the investigation of the small wavelength collective dynamics in liquids came with the progress of IXS over the last 10 years.

For liquid sodium close to its solidification temperature ($T_m = 371$ K) such spectra are exemplarily shown in figure 5. The data were obtained at the inelastic beamline ID16 of the ESRF in Grenoble [28]. Sound modes can clearly be identified in the scattering law up to about 0.75 Q_0 (not shown in the figure), where $Q_0 = 2.01$ Å^{-1} is the position of the main maximum in $S(Q)$. The Q-range is clearly beyond the hydrodynamic limit, which is characterized by $\sigma \cdot Q \approx 1$ and which can be estimated by employing the hard sphere diameter of liquid sodium [67] (σ_H(Na) = 3.34 Å). Following the definition, Q-values above 0.3 Å^{-1} lie clearly in the molecular dynamics domain.

The excitation frequencies of the modes are easily obtained from fitting a *damped harmonic oscillator model* (DHO) [54] to the data convoluted with the experimental resolution, where the quasielastic contribution is simulated by an additional Lorentzian (for the sake of clarity the DHO spectra are not displayed in figure 5). A characteristic Q–ω-relation is found which considerably differs from the hydrodynamic predictions, as is shown in figure 6. The

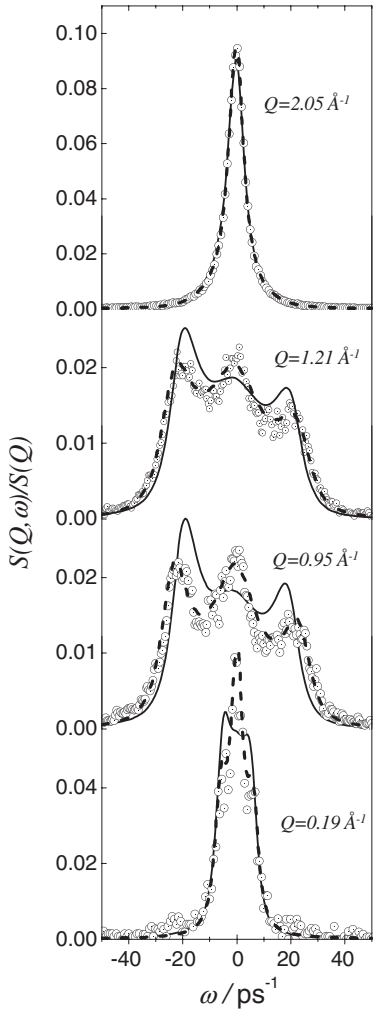

Figure 5. Selected $S(Q, \omega)$-spectra of liquid sodium at 380 K obtained from IXS. Open circles are experimental data, the full line corresponds to the viscoelastic model (equation (4.7)) in the Lovesey approximation, the dashed line the viscoelastic model with τ_L, $\omega_0(Q)$ and $\omega_L(Q)$ used as free fitting parameters.

excitation frequencies of the modes no longer increase simply linearly with Q as predicted by equation (4.1); instead, a similarity to the well known phonon dispersions of the corresponding crystalline solids is found: at lower Q the mode frequency increases about linearly, but with increasing momentum transfer the slope begins to decrease and finally vanishes at $\approx Q_0/2$. In the crystal this would correspond to the first Brillouin zone boundary, where, as a consequence of the interaction between the phonons and the translational invariance of the lattice, the phonons form standing, non-propagating waves. The full circles in figure 6 are results from an MD simulation [55] where an effective pair potential was used derived in a similar way as the potential given in equation (1.2), where, however, another empty core potential [56] was used and a different local field for the dielectric function [57]. The simulation result is in perfect agreement with the experimental data, indicating that this potential is well suited to describe the particle dynamics in this liquid alkali metal.

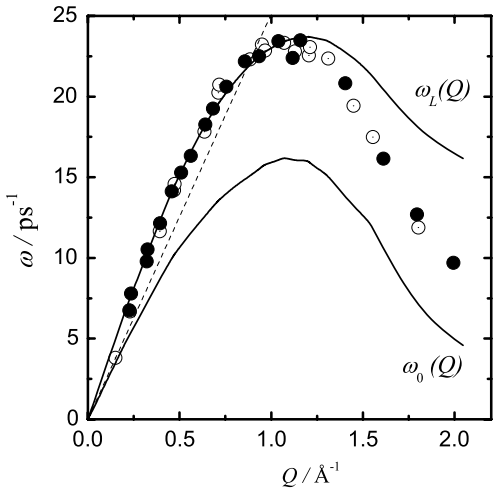

Figure 6. Q–ω-relation of the longitudinal collective excitations in molten sodium (380 K). Open circles are obtained from fitting the DHO model to the IXS data; closed circles are results of an MD simulation [55]; the slope of the dashed line is given by c_{T}. The full lines denote $\omega_0(Q)$ and $\omega_{\mathrm{L}}(Q)$ as calculated employing equations (3.15) and (3.16) with an appropriate effective potential [55] and experimental data [60], respectively.

For a molecular dynamics description of the scattering law beyond $\sigma Q \approx 1$ the hydrodynamic description needs to be modified. This is done in an approach which is called the *generalized hydrodynamics*. Speaking in terms of reciprocal space, the applicability of classical hydrodynamics is extended to values of the momentum transfer typical for inelastic x-ray or neutron scattering experiments.

Starting from the longitudinal part of the linearized Navier–Stokes equations one can derive a simple form of an equation of motion for the current density which defines the time dependence of the particle flow in the $Q \to 0$ limit [36]. This expression is then further refined for use beyond the hydrodynamic limit by introducing the relevant quantities in this relation as nonlocal Q-dependent functions. In particular, the longitudinal viscosity is generalized in the form of a memory function, which allows the expression of the complete equation of motion for the current density in a specific standard form for correlation functions, a so called generalized Langevin equation [58]:

$$\begin{aligned} &\frac{\partial}{\partial t} J_{\mathrm{L}}(Q,t) = -\int_0^t K_{\mathrm{L}}(Q,t-t') \cdot J_{\mathrm{L}}(Q,t')\,\mathrm{d}t' \\ &K_{\mathrm{L}}(Q,t) = \omega_0^2(Q) + Q^2\, M(Q,t). \end{aligned} \tag{4.4}$$

$M(Q,t)$ is the memory function for the density–density correlation which contains the exact details of the relaxation processes in the liquid. Equation (4.4) is 'exact' as long as we have not introduced a specific approximation for the memory function $M(Q,t)$. This is also the drawback of this approach because $M(Q,t)$ contains in some way the generalized thermal diffusivity $D_{\mathrm{T}}(Q)$ and the generalized viscosity $\Phi_{\mathrm{L}}(Q,t)$ for which we do not have a recipe for a straightforward determination. Hence, this function introduces some uncertainty and $M(Q,t)$ may therefore be viewed as a 'free' function, whose choice finally determines the consistency with experiment. The Laplace–Fourier transform of (4.4) returns $J_{\mathrm{L}}(Q, z = \mathrm{i}\omega)$ with real part $J_{\mathrm{L}}(Q,\omega)$, which determines the frequency spectrum of $J_{\mathrm{L}}(Q,t)$. For the scattering law one

then obtains

$$S(Q,\omega) = \frac{Q^2}{\omega^2} J_{\mathrm{L}}(Q,\omega)$$
$$= \frac{S(Q)}{\pi} \frac{Q^2\,\omega_0^2(Q) M'(Q,\omega)}{\left[\omega^2 - \omega_0^2(Q) + \omega\, Q^2 M''(Q,\omega)\right]^2 + \left[\omega Q^2\, M'(Q,\omega)\right]^2}. \tag{4.5}$$

$M'(Q,\omega)$ and $M''(Q,\omega)$ are respectively the real and imaginary part from the Fourier transforms of $M(Q,t)$ and responsible for damping and dispersion of the collective modes.

The simplest approach to a suitable scattering law is to assume that $M(Q,t)$ can directly be identified with the viscosity function $\Phi_{\mathrm{L}}(Q,t)$, neglecting thermal diffusion and implying that viscous dissipation is the only relaxation channel in the liquid. Furthermore, one may presume that the decay occurs simply exponentially with characteristic decay time $\tau_{\mathrm{L}}(Q)$:

$$M(Q,t) \equiv \Phi_{\mathrm{L}}(Q,t) = \Phi_{\mathrm{L}}(Q,0)\mathrm{e}^{-t/\tau_{\mathrm{L}}(Q)}. \tag{4.6}$$

The use of (4.6) was in fact motivated by a similar approach to describe transverse modes in Lennard-Jones systems [44]. The initial value of the generalized longitudinal viscosity $\Phi_{\mathrm{L}}(Q,0)$ can be determined from a comparison with sum rules [36], allowing the ready computation of the real and imaginary parts of $M(Q,t)$, and after some algebra one obtains

$$\frac{S(Q,\omega)}{S(Q)} = \frac{1}{\pi} \frac{\tau_{\mathrm{L}}(Q)\omega_0^2(Q)\left[\omega_{\mathrm{L}}^2(Q) - \omega_0^2(Q)\right]}{\left[\omega\tau_{\mathrm{L}}(Q)\left(\omega^2 - \omega_{\mathrm{L}}^2(Q)\right)\right]^2 + \left[\omega^2 - \omega_0^2(Q)\right]^2}. \tag{4.7}$$

Due to the physical prerequisites put into the model, (4.7) is called the *viscoelastic approximation*. In this simple approach the scattering law is fully determined by the information put into the frequency moments and by $\tau_{\mathrm{L}}(Q)$ as an adjustable parameter. In his derivation of (4.7) [59] Lovesey has suggested that the latter can directly be related to $\omega_0(Q)$ and $\omega_{\mathrm{L}}(Q)$, leaving (4.7) without any free parameter, and the scattering law can straightforwardly be calculated from the frequency moments, i.e. from a knowledge of the static liquid structure and the underlying pair potential. The results of such a calculation are shown in figure 5 as the full lines. Waseda's $S(Q)$-data [60] and the pair potential used to compute the dispersion relation in figure 6 [55] were employed as an input. Although the three line structure of the experimental result is nicely reproduced, the agreement with the measured data remains poor. However, the situation can considerably be improved if (4.7) is used as a fitting function with $\tau_{\mathrm{L}}(Q)$, $\omega_0(Q)$ and $\omega_{\mathrm{L}}(Q)$ as free parameters. Results from this procedure are also shown in figure 5 as the dashed lines. The agreement with experiment improves considerably. However, employing such a data analysis one carefully needs to confirm that the parameters remain physically. Their Q-dependence, as obtained from the fitting, is shown in figure 7 together with the direct calculation of the corresponding functions. Although the spectra obtained from the Lovesey model and from the fitting procedure differ considerably, the differences between the parameters remain small, indicating on one hand the sensibility of (4.7) and the fact that the Lovesey model is not unreasonable and viscous relaxation may in fact play the dominant role. Nevertheless, this *single exponential model* has several drawbacks: the agreement with experiment is not perfect. A closer inspection of figure 5 reveals that especially the central line is not fully reproduced although the deviations fade with increasing Q towards the structure factor maximum, i.e. with diminishing influence from the collective excitations. More confusing, however, is the fact, that—in contrast to the hydrodynamic view—a clear picture for the microscopic processes in the liquid does not evolve from this kind of memory function approach. No direct relation is obtained between e.g. the lifetime of a mode and the decay time $\tau_{\mathrm{L}}(Q)$ of the density–density correlation. This lack of information hampers a detailed understanding of the microscopic processes causing the observed three line structure.

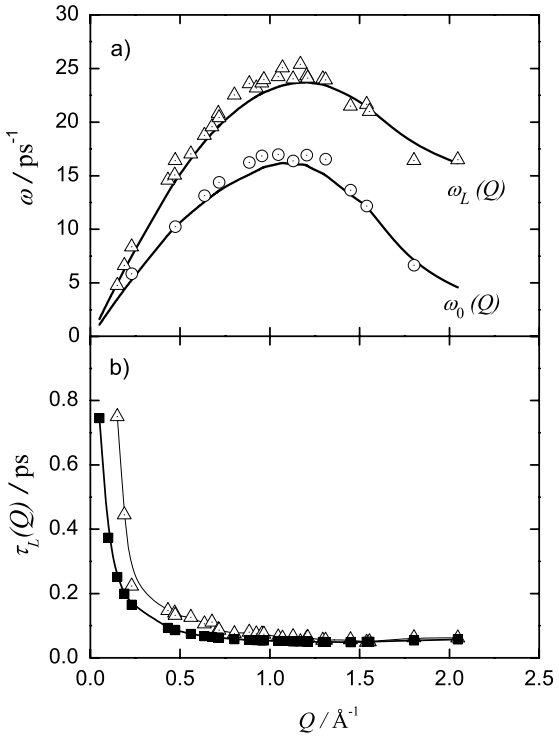

Figure 7. (a) Comparison of $\omega_0(Q)$ and $\omega_L(Q)$ as computed using $S(Q)$ [60] and an appropriate pair potential [55] in (3.15) and (3.16) (solid lines) with results from fitting (4.7) to the experimental data (circles and triangles). (b) Comparison between $\tau_L(Q)$ as obtained from the Lovesey model (■) and from fitting (4.7) to the data (△).

Apparently, a clear assignment of distinct relaxation mechanisms to distinct excitations is not as simple on the microscopic scale. It must also be emphasized that dissipation due to thermal conduction is not taken into account. The memory function formalism can also be used to derive the hydrodynamic scattering law [36]. In that case, the thermal diffusivity appears in an additional exponential to the viscous term in the memory function. Extending this expression to a generalized hydrodynamic description gives [36]

$$M(Q,t) = \omega_0^2(Q) + Q^2\Phi_L(Q,t) + \omega_0^2(Q)(\gamma - 1)e^{-D_T Q^2 t}. \tag{4.8}$$

However, for the alkali metals a big improvement is not to be expected. Due to the higher Q considered here and the large thermal conductivities of the alkali metals the exponential has already declined to negligible values. Additionally, in this extension of the hydrodynamic view the thermal diffusivity is still weighted by $\gamma - 1$, which for the alkalis is very small and furthermore reduces the weight of this term.

Although the observed three line structure can apparently be described with a single relaxation process, it was shown in the past that it is more sensible to assume the existence of a second viscosity related mechanism. This was observed for the first time by Alder and Wainwright [61] in a computer simulation on hard spheres, where two processes could be distinguished in the stress–stress correlation function: a rapid initial decay due to random binary collisions and an additional long time decay due to *viscoelastic* effects. The neglect of the second contribution led to a severe underestimate of the shear viscosity. A similar observation was made in another MD work by Levesque *et al* [44] in the attempt to correctly

describe the decay of the memory function for the transverse current correlation. It appears hence obvious to try a similar strategy here and $M(Q,t)$ may then take the form [36]

$$M(Q,t) = \omega_0^2(Q) + \left[\omega_L^2(Q) - \gamma(Q)\omega_0^2(Q)\right]\left\{(1-\alpha(Q))\,\mathrm{e}^{-t/\tau_\alpha(Q)} + \alpha(Q)\mathrm{e}^{-t/\tau_\mu(Q)}\right\} + \omega_0^2(Q)\,(\gamma(Q)-1)\,\mathrm{e}^{-D_T(Q)Q^2t}. \tag{4.9}$$

Here, $\alpha(Q)$ denotes the relative weight of the respective viscous contributions. Additionally, the thermal diffusivity and the ratio of the heat capacities have been generalized by allowing for a corresponding Q-dependence. Using $\tau_\alpha(Q)$, $\tau_\mu(Q)$, $\alpha(Q)$, $D_T(Q)$ and $\gamma(Q)$ as fitting parameters it was shown that the *two relaxation time model* fits very well to molecular dynamics data of Lennard-Jones systems [44].

Excellent agreement to experiment could also recently be obtained by employing this idea in a fitting procedure, with D_T and γ left as constants, to reproduce very precise $S(Q,\omega)$-measurements on dense liquid lithium [62] and sodium [63]. For molten sodium some results of this analysis are shown in figure 8 as the thicker lines. The data are now in perfect agreement with experiment. The thin line in the figure corresponds to a fitting process with only one exponential, i.e. to the conventional *viscoelastic model*. A distinct difference is found between the two methods, indicating that the use of a second viscous relaxation mechanism seems to be appropriate. The Q-dependence of the two relaxation constants is depicted in figure 9. In accord with the observation by Alder and Wainwright [61], two processes on distinctly different timescales can indeed be identified: one relaxation time denoted τ_μ corresponds to a fast decay of the density correlation while another process, denoted by τ_α, occurs on a timescale about one order of magnitude slower. This implies that the fast decay is the main contribution determining the shape of the memory function. The notations μ and α for the relaxation channels were chosen to point to a similarity in the analysis of light scattering spectra from glass formers where the use of a two exponential viscous model is customary (see e.g. [64]). In fact, there exist current attempts to relate the two time constants directly to those of an undercooled glass forming liquid [65], implying a continuous transition from the liquid to the disordered solid phase.

Interestingly, the fast process has the same timescale as $\tau_L(Q)$ obtained from the *viscoelastic model*. Moreover, it is found that the weight of this process dominates considerably, indicating that it mainly determines the main features in $S(Q,\omega)$.

Valuable information on the microscopic dynamics in a liquid can also be gained directly from the shape of the dispersion relation: in the low Q limit the excitations propagate either with adiabatic or with isothermal speed of sound. However, figure 6 indicates that the slope of the dispersion relation in the lower Q range is considerably larger (the dashed line gives the expected behaviour due to c_T).

The small wavelength modes apparently travel faster than their hydrodynamic counterparts. This effect is also a clear deviation from the hydrodynamic prediction which sets in close to the aforementioned limit estimated to lie at about 0.3 Å^{-1}. It is interesting to note that the mode indicated by the symbol at $Q = 0.19$ Å^{-1} in figure 6, a Q-value which was formally estimated to still lie within the hydrodynamic regime, in fact propagates with adiabatic or isothermal speed of sound. The question of the transition from hydrodynamics to molecular dynamics has already been addressed some years ago in a neutron Brillouin experiment on compressed fluid argon, where the bending up of the dispersion curve could directly be measured [66].

The effect can also be understood within the context of generalized hydrodynamics. Discussing the denominator in equation (4.5) [36] it is shown that—depending on frequency—two limits exist for the dispersion relation and hence for the phase velocity of the modes: at low frequency, i.e. when the condition $\omega\tau \ll 1$ is valid, the Q–ω-relation is given by

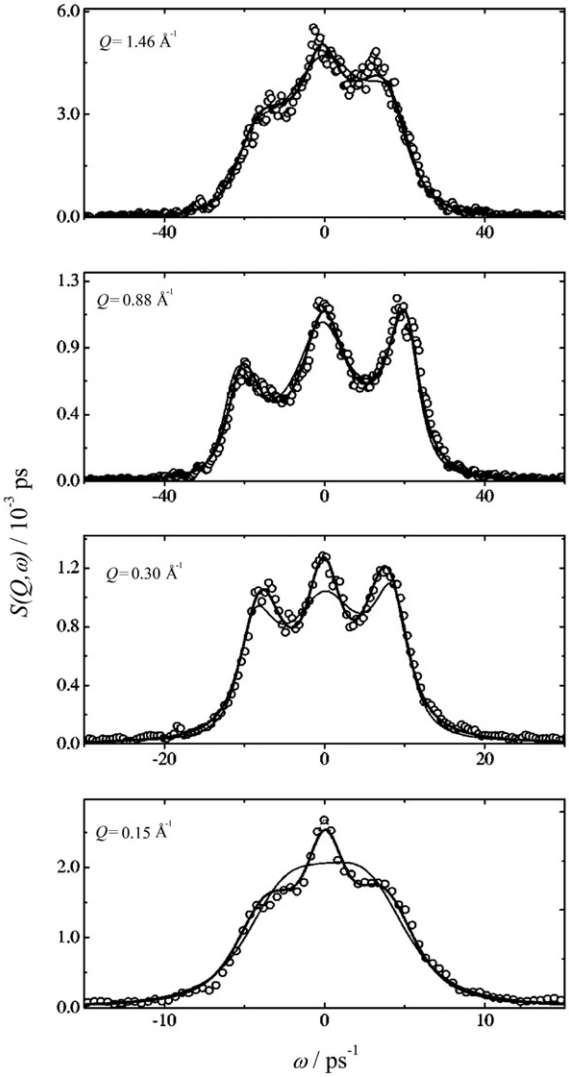

Figure 8. Some selected spectra of an IXS investigation on molten sodium [63]. The thin lines represent the results from fitting (4.7) to the data with $\tau_L(Q)$ as a free parameter. The thick lines are results from a fitting procedure where a two exponential model similar to equation (4.9) was employed for $M(Q, t)$.

$\gamma\omega_0(Q)$, i.e. basically by the normalized second moment. In this case the modes oscillate much slower than the characteristic decay of the density–density correlation imposed onto a volume element in the liquid by a compression–dilation cycle of the traversing excitation. One may then define a low frequency sound speed $c_0(Q) = \gamma\omega_0(Q)/Q$, which in the $Q \to 0$ limit reduces to the adiabatic speed of sound c_S, i.e. to the correct hydrodynamic prediction. If, however, the frequency is sufficiently high, i.e. if $\omega\tau \gg 1$, the density correlation imposed by an oscillating mode has no time to decay. Then elastic shear and compression moduli originate, determining the dynamical behaviour of a microscopic volume element. This causes a shift to higher frequency leading to the observed rise in phase velocity. The dispersion relation is

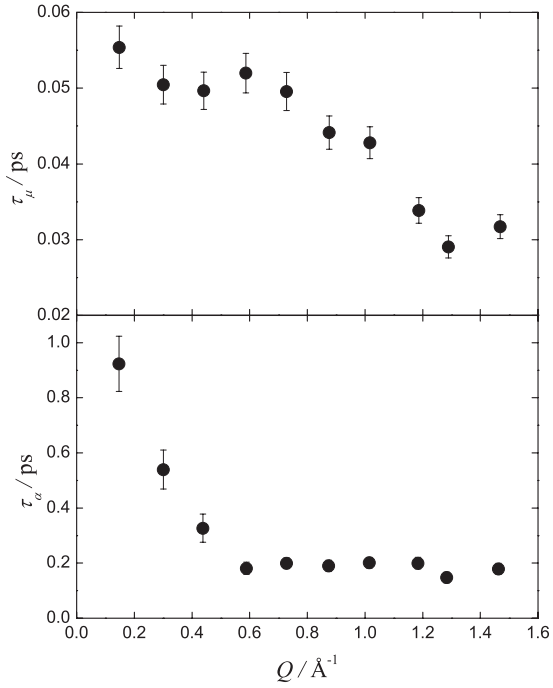

Figure 9. Q-dependence of the relaxation times τ_μ and τ_α for liquid sodium close to melting, obtained from fitting the two relaxation time model (equation (4.9)) to experimental IXS data [63].

then given by $\omega_L(Q)$ [36], which is in fact observed in the experiment (see figure 6). In this limit one may again define a propagation speed $c_\infty(Q) = \omega_L(Q)/Q$. The Q-dependence of the phase velocities is depicted in figure 10(a). Open circles correspond to measured data $c_m(Q) = \omega_m(Q)/Q$ while the solid lines give $c_0(Q)$ and $c_\infty(Q)$ computed from $\omega_0(Q)$ and $\omega_L(Q)$ of figure 6, respectively.

Two things seem mainly to be responsible for the deviation of the Q–ω-relation from the hydrodynamic prediction with increasing Q and hence for the departure of the mode velocity $c_m(Q)$ from the bulk value: firstly, the increasing interaction of the mode with the microscopic structure leading to a bending down of the Q–ω-relation and the formation of the quasi-Brillouin-zone boundary at $\approx Q_0/2$. To a first approximation, this behaviour is reproduced by the second normalized frequency moment containing the structural information via $S(Q)$. Additionally, a second rather dynamical contribution becomes important with rising frequency. It is related to the onset of quasi-elastic restoring forces and hence reflects the short range interactions in the liquid. As a result, a bending up of the dispersion relation towards $\omega_L(Q)$ is found, causing an increase of the phase velocity. It is challenging to ask for a microscopic understanding of the latter effect. As a first attempt one may try to simply subtract the structural contribution represented by $c_0(Q)$ (or $\omega_0(Q)$) from the experimental phase velocity. For sodium the result is shown in figure 10(b).

A sharply peaking function is obtained with a pronounced maximum at $Q^* \approx 0.63$ Å^{-1}. At this Q-value the dynamic influence on the dispersion relation seems to have its largest contribution. Estimating the corresponding r-space value as $r^* = 2\pi/Q$ gives 9.9 Å, which exactly matches three hard sphere diameters (σ_H(Na) = 3.36 Å [67]). Apparently, the observed onset of quasielastic solid-like forces at sufficiently high frequency, i.e. at sufficiently small

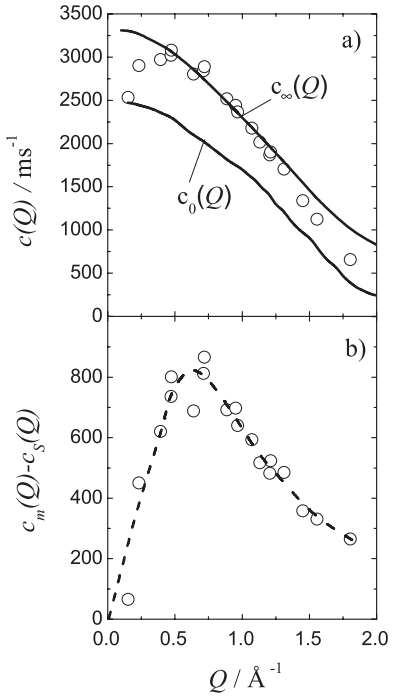

Figure 10. (a) Measured phase velocity $c_{\rm m}(Q)$ of the collective modes in liquid Na at 388 K (open circles), Q-dependent adiabatic sound velocity $c_0(Q)$ and high frequency limit $c_\infty(Q)$ (solid lines). (b) Difference between phase velocity $c_{\rm m}(Q)$ of the collective modes and the adiabatic sound velocity $c_{\rm S}(Q)$. Dashed line: computer spline.

wavelength, can structurally be related to inhomogeneities with diameter ≈10 Å. Interestingly, $r^*/2$ coincides exactly with the first minimum in the pair correlation function $g(r)$ [60], as is illustrated in figure 11. Moreover, integrating the radial distribution function $4\pi r^2 g(r)$ up to this value yields that the corresponding volume contains 12.5 atoms. Hence, we identify the underlying structural inhomogeneities as the shell of next neighbours around a central ion, the most stable structural arrangement in the otherwise disordered melt. In order to confirm that these findings from molten Na are not accidental, we have undertaken the same analysis using older $S(Q, \omega)$-data on molten caesium [68]. Here, a value of $r^* = 14.5$ Å is found, which is again three times the hard sphere diameter of the ion ($\sigma_{\rm H}$(Cs) = 4.76 Å [67]). Also, $r^*/2$ and the first minimum in $g(r)$ coincide, and an appropriate integration yields 13 ions in this case. The characteristic number of particles found from integrating the radial distribution function tempts further speculation that the underlying structural arrangements are of icosahedral order, for which 12 ions would reside around a central particle. Similar conclusions were drawn for liquid rubidium from a discussion of the bond angle distribution obtained from an MD simulation [69]. In fact, it has been known for a long time that the formation of icosahedral aggregates is associated with a distinct decrease in interaction energy [70].

4.3. Temperature dependence of the collective dynamics

The dense liquid alkali metals show a distinct solid-like character: the particle dynamics is subject to collective phononic excitations extending down to microscopic wavelengths with

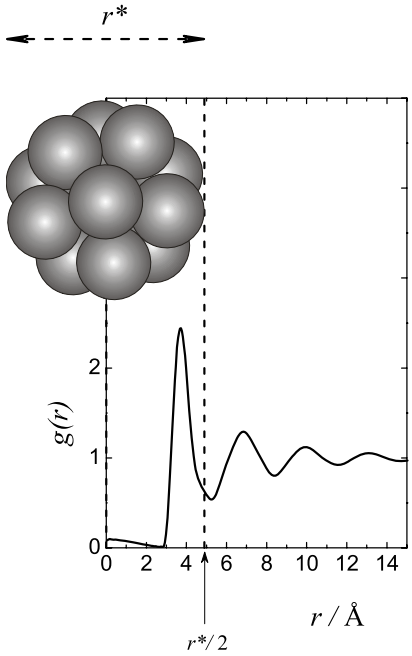

Figure 11. Pair correlation function $g(r)$ for liquid Na [60]. The first minimum matches with the radius $r^*/2$ of the concluded shell of next neighbours.

a solid-like dispersion relation. At high mode frequencies the liquid develops internal shear and compression moduli similarly as in a solid, causing an increase of the propagation speed towards the value of the crystal where the sound velocity is larger than in the liquid. These observations were often regarded as reminiscent of the nearby solid state. Thus, the solid-like properties were supposed to be present only in the vicinity of melting [36, 71]. We examined this assumption in extending our experiments to higher temperatures [28]. The temperature variation of the scattering law is exemplarily shown in figure 12 for a spectrum at $Q = 1$ Å^{-1}.

Similarly as in figure 5, the solid lines are fits employing equation (4.7) with $\omega_0(Q)$, $\omega_L(Q)$ and $\tau_L(Q)$ as free parameters, while the dashed lines correspond to the direct calculation of the viscoelastic model employing structural data [60] and the pseudopotential mentioned above [55]. The variation of the dispersion relations with rising temperature is shown in figure 13. No characteristic changes in the collective dynamics are found. The viscoelastic model can still be fitted to the spectra (figures 12(a)–(d)). $\tau_L(Q)$ is found to slightly decrease, leading to an overall broadening of the spectra with rising T. The dispersion relations also do not vary much compared to melting (see figures 13(a)–(d)). A positive dispersion is found at all temperatures, indicating that elastic solid-like restoring forces control the microscopic dynamics even at conditions which are far away from the solid phase.

It must however be emphasized that the temperature and density range explored in the experiments on molten sodium were not extended to conditions where the view of a delocalized electron gas may no longer be appropriate, i.e. down to liquid densities below $3\rho_{crit}$. The interparticle forces within the liquid are hence still controlled by the delocalized electrons. It is therefore sensible to relate the observed solid-like behaviour rather to the specific metallic binding in the liquid than to the thermophysical vicinity of the solid crystalline phase.

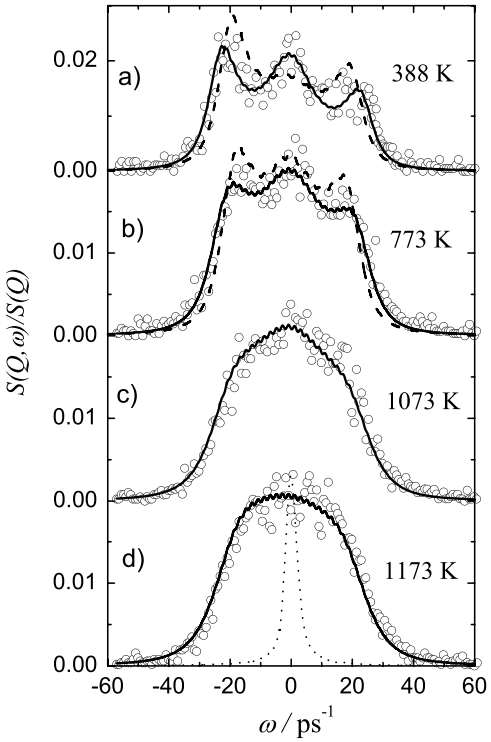

Figure 12. $S(Q, \omega)$ of molten Na for different temperatures. Open circles correspond to experimental data [28], the solid line is a fit of the viscoelastic model (equation (4.7)), and the dashed lines represent direct calculations using a characteristic pair potential [55] and structural data [60] as inputs (no such data exist for the higher temperatures). The dotted line shows the experimental resolution function.

4.4. The expanded liquid metal

So far we have assumed that the fluid alkali metals were monatomic and the forces between the particles were unambiguously determined by a dense gas of delocalized electrons. The interparticle potential can then adequately be described within the framework of pseudopotential theory. However, as already mentioned in the introduction, this is no longer the case if the density of the liquid is sufficiently reduced. Then, the screening of the ions breaks down and the electrons start to localize. Measurements on the density dependence of the electronic and magnetic properties of the molten alkalis indicate that this scenario sets in below $3\rho_{\text{crit}}$. This is exemplarily illustrated in figure 14, for the dc electrical conductivity of fluid caesium. Full circles correspond to measurements which were carried out for a number of states along the liquid–vapour coexistence curve [72]; open circles represent calculations within the framework of the *nearly free electron* (NFE) model, where the conductivity is related to the structure of the liquid, i.e. to the static structure factor $S(Q)$, by the well known Faber–Ziman formula [73]. The model hence represents the pure influence of density without any further electronic effect. For the computations [74], experimental $S(Q)$-data [75] were used as an input. At high density, calculations and measurements are in perfect agreement. However, since the model ignores localization the two datasets diverge when this effect becomes dominant below $3\rho_{\text{crit}}$. A similar scenario is depicted in figure 15, which shows the density dependence of the magnetic mass susceptibility χ_g for the same metal [76]. A steep rise of χ_g is observed with decreasing ρ when

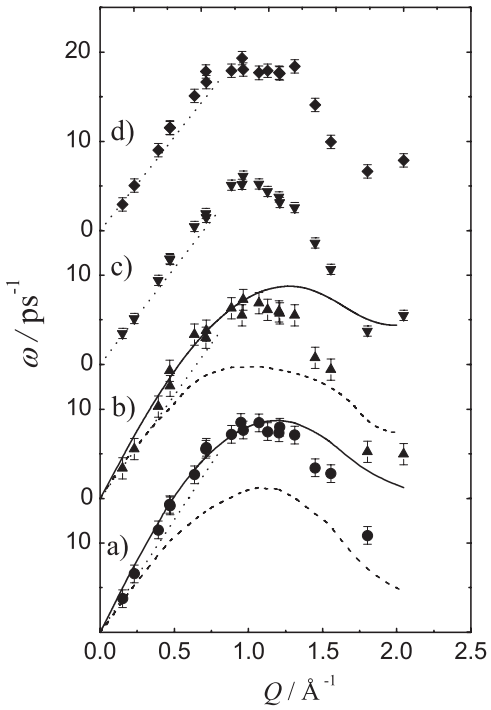

Figure 13. Dispersion relations of the collective excitations in molten Na for the temperatures given in figure 12 obtained from fitting the DHO model to the data. Dotted lines represent dispersion due to the isothermal speed of sound, dashed lines show $\omega_0(Q)$ and full lines give the $\omega_L(Q)$ curves, which were calculated using an adequate pair potential [55] and structural data [60] (see also figure 6).

values below three times the critical density are approached, indicating the increasing number of unpaired spins which have localized at their parent ions.

Above, it was already assumed that the continuous breakdown of the screening and the associated localization of the conduction electrons must also have a strong impact on the interparticle forces. As a consequence, considerable changes in the structural and in the dynamical features of the fluids should be expected. This interesting question was addressed in a variety of $S(Q)$- and $S(Q, \omega)$-investigations on fluid caesium [75] and rubidium [77, 78, 16], spanning nearly the whole liquid range between melting and the liquid–vapour critical point. Rubidium and caesium were chosen because of their lower critical temperatures and pressures as compared to the less heavy alkalis, a prerequisite to make such experiments feasible. It is found that the principal features of $S(Q, \omega)$ are similar to those already reported above for liquid sodium. Again, distinct collective excitations are observed in the coherent INS spectra extending up to momentum transfers beyond $Q_0/2$ [29, 68], which exhibit all of the above mentioned properties [71, 79]. Moreover, it was shown that the dispersion relations of all the dense liquid alkalis even collapse onto one universal Q–ω-relation [80] if appropriately scaled.

As already shown in figure 12, the characteristic three-line structure of the spectra gets continuously lost due to an overall broadening with rising temperature and decreasing density. Figure 16 depicts this situation for Rb showing $S(Q, \omega)$- and $J_L(Q, \omega)$-spectra at $Q = 1.3$ Å^{-1} for different thermodynamic states of the hot fluid. The data were obtained from high temperature INS investigations [18]. The reduced densities ρ/ρ_{crit} and hence the

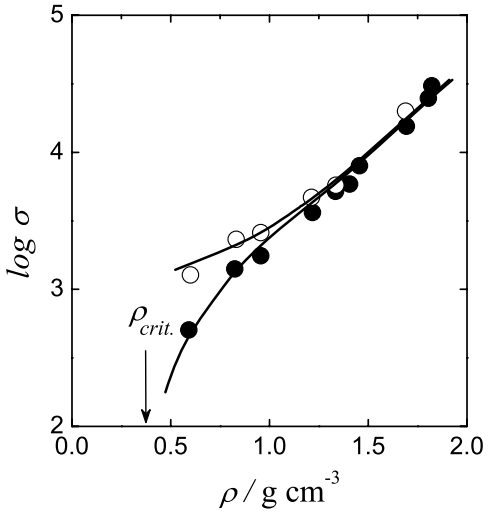

Figure 14. Dc conductivity in liquid caesium as a function of density along the liquid–vapour coexistence curve: ○, calculated values using Faber–Ziman theory [73]; ●, experiment [72]. Lines serve as guides for the eye.

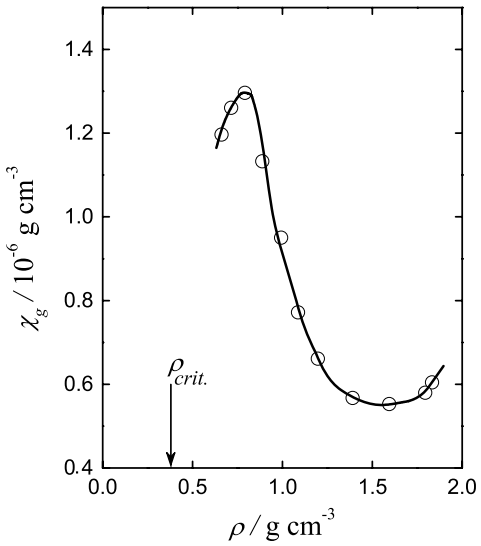

Figure 15. Mass susceptibility of liquid caesium measured along the liquid–vapour coexistence line [76]. The line serves as a guide for the eye.

particle densities are now even smaller than for the states presented in figures 12 and 13 for sodium but the condition $\rho \geqslant 3\rho_{\mathrm{crit}}$ still holds. However, the spectra show no unusual properties. $J_{\mathrm{L}}(Q, \omega)$ is simple shaped, comprising one distinct maximum as is expected for a conventional monatomic fluid. The collective excitations are highly overdamped and there is no more chance to obtain information on the collective excitations directly from $S(Q, \omega)$, i.e. a dispersion relation for the collective excitations can no longer be obtained from the scattering law. However, a dispersion relation of the current–current correlation is easily constructed. For some temperatures such functions are shown in figure 17. They show an oscillatory behaviour

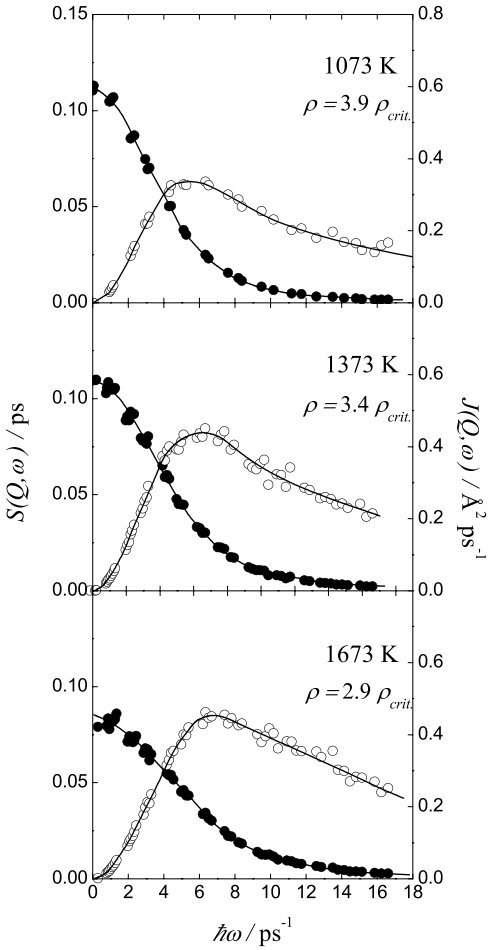

Figure 16. $S(Q,\omega)$ (●) and $J_L(Q,\omega)$ (○) of liquid rubidium for different temperatures close to the liquid–vapour coexistence curve [85]. The solid lines in the figure serve just as a guide to the eyes.

which fades with rising temperature and the frequency more and more increases monotonically with Q. Gradually, the curves approach the free gas limit where ω is directly proportional to the momentum transfer (as can easily be shown from equation (5.6)) if the temperature is raised.

The dispersion relations show a distinct minimum around Q_0, the position of the structure factor maximum, indicating that velocities of neighbouring particles are correlated. In other words, in reciprocal space one observes a general slowing down of the particle dynamics around the main peak in $S(Q)$. For the quasielastic line which represents the diffusive dynamics of the particles this is well known as the so called de Gennes [82] narrowing. With increasing temperature and correspondingly decreasing density the minimum shifts to smaller Q, representative of a slight increase of next neighbour distances. Also, the minimum gradually disappears, indicating the continuous loss in velocity correlation due to increasing temperature and decreasing density, as is expected in approaching the free gas limit. The first maximum of all the dispersion relations has a value of about 5 meV. The corresponding Q-value symbolizes the first quasi-Brillouin zone boundary. This point in reciprocal space

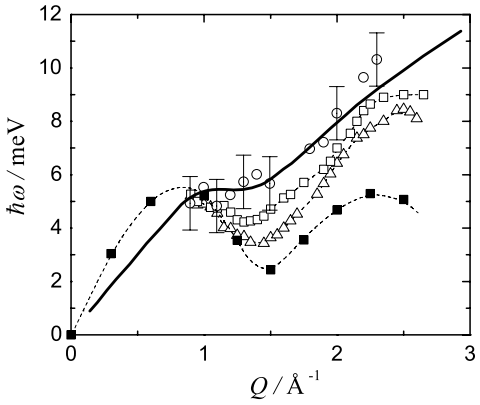

Figure 17. Dispersion of the longitudinal current correlation for some explored thermodynamic states: ■, 320 K; △, 1073 K; □, 1373 K; ○, 1723 K. The data at 320 K are taken from literature [29]; the data at the higher temperatures are taken from [81]. The dashed lines serve as guides for the eye; the solid line corresponds to a calculation [83] at 1700 K.

represents next neighbouring ions moving in an out of phase oscillatory motion. The associated frequency value can hence be viewed as a measure of the interparticle forces between next nearest neighbours in the liquid. This value does not change during expansion, indicating that the particle interactions remain essentially unchanged, i.e. the forces between the ions are still controlled by the metallic binding from the delocalized electrons along the temperature/density range displayed in figure 17. The observed variation in the curves is hence a pure temperature and density effect and there are no indications for a characteristic variation of the particle potentials due to a reorientation of the electronic density distribution. The solid line in figure 17 shows the result of a calculation at 1700 K [83] where the viscoelastic model (equation (4.7)) was employed together with $S(Q)$ obtained from a hypernetted chain approach. As already discussed above the viscoelastic model is representative of a monatomic simple liquid. The agreement between the calculation and the measured 1727 K data is hence another indication that the dynamical features of the high temperature fluid have still the same origin as under melting point conditions. Electron localization has not yet the dominant influence on the short range correlations.

If the density is further decreased and values close to twice the critical value (0.61 g cm^{-3}, 1873 K) are approached, drastic changes are observed in $S(Q,\omega)$ and consequently in $J_{\mathrm{L}}(Q,\omega)$. A well defined peak appears in the scattering law centred around 3.2 meV with maximum intensity at about 1 Å^{-1}. The corresponding spectra are shown in figure 18. Their shape is now in great contrast to the findings at higher density and lower temperature (see figures 12 and 16).

The distinct shoulder in $S(Q,\omega)$ is only visible along a narrow Q-range, which is consistent with a simple model for an assembly of non-interacting diatomic harmonic oscillators [6, 37]. For temperatures as high as 1873 K the model has the simple form

$$S(Q,\omega) = \sum_{n=-\infty}^{\infty} I_n(y)\mathrm{e}^{-y}\delta(\omega - n\omega_0) \qquad \text{with } y = \frac{\hbar^2 Q^2 k_{\mathrm{B}} T}{M(\hbar\omega_0)^2}. \tag{4.10}$$

Here, the $I_n(y)$ are modified Bessel functions of the first kind and nth order, $\hbar\omega_0$ is the energy difference between adjacent energy levels of the oscillating particle and the δ-function under the sum ensures energy conservation during the interaction between the neutron and the molecule. Inserting the observed value of 3.2 meV and the reduced mass M for a rubidium dimer yields

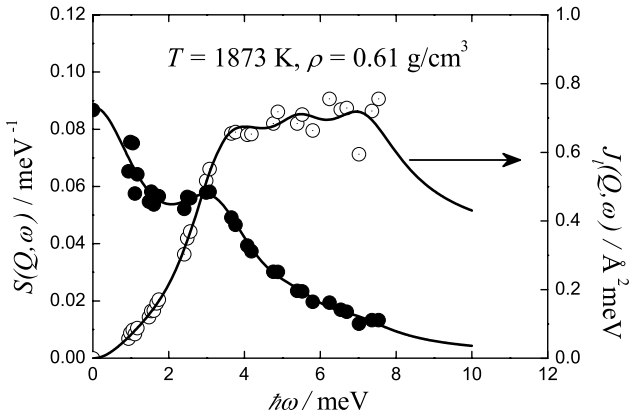

Figure 18. Experimental $S(Q,\omega)$ and $J_L(Q,\omega)$ for fluid rubidium at $Q = 1$ Å^{-1} for $\rho \approx 2\rho_{crit}$ (1873 K). Data are taken from [7]. The solid lines are the result from fitting a set of three Lorentzians to the data.

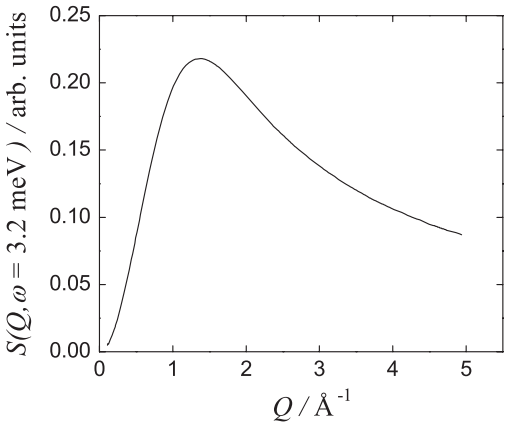

Figure 19. Q-dependent intensity for a peak in $S(Q,\omega)$ resulting from a vibron excitation of a Rb_2 dimer at 3.2 meV and a temperature of 1873 K (equation (4.10)).

the Q-dependence of the excitation intensity, which is shown in figure 19. In fact, the peak corresponding to the vibrational excitation (vibron) of such a particle shows a distinct maximum in Q-space, which is centred around $Q = 1$ Å^{-1}, in accord with the experimental finding. This analogy makes it tempting to speculate that molecular aggregates of some sort may form in the dilute fluid, consisting of atoms performing out of phase oscillations similarly as in a Rb_2 dimer, which is well known to exist in the gas phase. This interpretation is also consistent with the density dependence of the mass susceptibility in figure 15. While χ_g increases with decreasing density below $3\rho_{crit}$, an additional decline is observed beyond twice the critical density, which can be interpreted as resulting from spin pairing due to the formation of molecular aggregates with localized bonds.

The peak in the scattering law can also be identified in $J_L(Q,\omega)$, where higher harmonics are also indicated (see figure 18). The pattern in the current correlation spectra (and consequently in $S(Q,\omega)$) can be nicely reproduced using a set of three Lorentzians, one for the quasielastic contribution and two to model the excitation and its first harmonic (solid lines in figures 18).

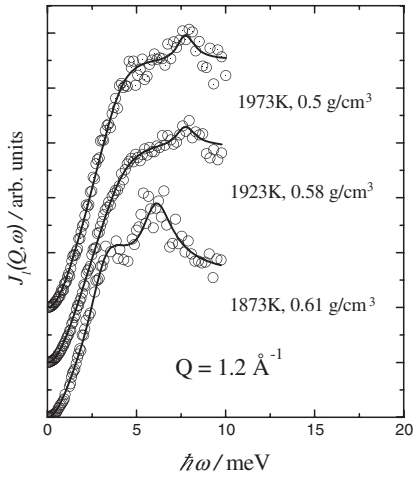

Figure 20. Current correlation spectra of fluid rubidium at 1873, 1923 and 1973 K and $Q = 1.2$ Å^{-1} [81]. Distinct excitations are visible, superimposing $J_L(Q, \omega)$. Solid lines are fits of three Lorentzians to $S(Q, \omega)$.

If the temperature is further raised additional variations are observed. The peak in $S(Q, \omega)$ is no longer visible, while the pattern in the current correlation functions remains. It is visible over a wider Q-range from ∼0.8 Å^{-1} to ∼1.4 Å^{-1} with a maximum intensity at 1–1.2 Å^{-1}. As examples, figure 20 shows current correlation spectra at 1.2 Å^{-1} for densities $\rho \leqslant 2\rho_{\text{crit}}$, at temperatures of 1873, 1923 and 1973 K, respectively. Again, the solid lines represent fits of a set of three simple Lorentzians to the data. No dispersion of the excitations is found, which again can be valued as an indication of the localized nature of the vibron. However, a slight shift to higher frequency with rising T is observed.

In order to get additional theoretical support for the suspected molecular species responsible for the observed pattern, exploratory calculations employing a simple model were undertaken: the total energy of expanded lattices for monatomic Rb and Rb_2 dimers at 0 K were carried out, using density functional theory (DFT) in the local density approximation (LDA) [84–86].

Calculations were made for a system of Rb atoms in a body-centred lattice (bcc) and for diatomic molecules in a simple cubic lattice (sc). To create the diatomic solid the two atoms in the bcc unit cell were moved towards each other, forming a simple cubic lattice (sc). The lattices were then continuously expanded and the total energy was calculated for several densities, also taking into account the dimer bond length in the molecular lattice, which was varied for energy minimization. It was found that for densities below 0.9 g cm^{-3} the molecular lattice has the lower energy. Interestingly, this is again about $\sim 3\rho_{\text{crit}}$ of the corresponding fluid. From the bond length variation the oscillator potential could be obtained along the explored density range. A Morse potential [87] was then fitted to these functions, giving the density dependence of the vibron energy, $\hbar\omega_0$, and the respective dissociation energy. Figure 21 shows the density variation of the vibron energy obtained from this procedure (open squares). The experimental point in the gas at $\rho = 0$ g cm^{-3} [88] connects smoothly with the calculations at higher density. Also shown in figure 21 are the experimental vibron energies taken from the spectra in figure 20, which are in good agreement with the calculations.

The dissociation energy is also found to decrease with increasing density from the gas phase value down to zero near 0.9 g cm^{-3}. The decrease of the vibron and dissociation energy

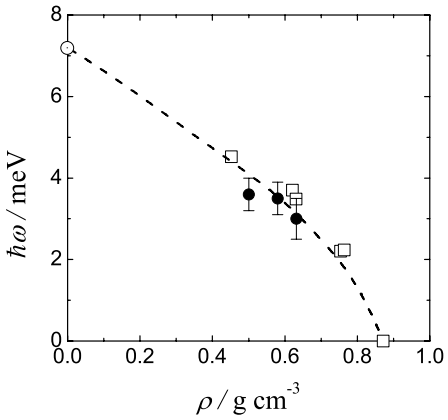

Figure 21. Density variation of the vibron energy $\hbar\omega_0$ for Rb_2 in a molecular crystal [81]: □, DFT calculation; ●, experimental data; ⊙, Rb_2 vibron from the gas phase [88]. The dashed line serves as a guide for the eye.

with rising ρ is nowadays a well established feature, also found in optical studies on solid molecular hydrogen [89] and nitrogen [90]. It is believed to be associated with the transfer of electron charge towards neighbouring molecules, leading to a softening of the molecular bond and the formation of a monatomic state.

The variations in the scattering law which are observed when the density of a liquid alkali metal is reduced to values below $3\rho_{\mathrm{crit}}$ are indisputable and there is no question that they must be related to the localization of the conduction electrons and the associated change in the interparticle interactions. We have also seen that some simple models are able to describe the observed phenomena implying the formation of molecular structures in the expanded hot fluid. Apparently, the pattern observed in $S(Q,\omega)$ and in $J_{\mathrm{L}}(Q,\omega)$ results from an out of phase oscillation of bound atoms in such aggregates, similarly as in dimer molecules, which are well known from the dilute alkali vapours. However, there are still some incongruities which hamper a quantitative understanding of the density dependent microscopic processes. For instance, the ongoing variation of the scattering law with further decreasing density below 0.61 g cm^{-3} towards ρ_{crit} remains incomprehensible (e.g. the disappearance of the shoulder in $S(Q,\omega)$). A possible explanation could be that two competing effects must be taken into account: while the progressing localization of conduction electrons supports the formation of molecular structures the associated rise in temperature favours dissociation. However, this gives no quantitative explanation for the observation why in contrast to the $S(Q,\omega)$-spectra the pattern in the current correlation spectra remains visible along the whole explored density range. It is rather sensible to assume a continuous density dependence of the specific molecular structures which after sufficient expansion may transform into the well known dimer states.

Additionally, the models used to describe the observed features are highly oversimplified, e.g. the DFT calculations on the Rb solids were carried out at 0 K disregarding thermal effects, whereas it has already been mentioned in the introduction that temperature plays an important role regarding the composition of the fluid.

In order to unravel the temperature and density dependent processes on the microscopic level in more detail, a variety of intensive computer simulations were carried out. Kahl and Kambayashi [91] have tried to reproduce the shape of the scattering law of liquid rubidium in MD simulations employing interatomic potentials based on pseudopotential theory. In the lower and intermediate temperature range they found good agreement between the calculations and the experimental data. The simulations were extended to 1873 K; however, they were not

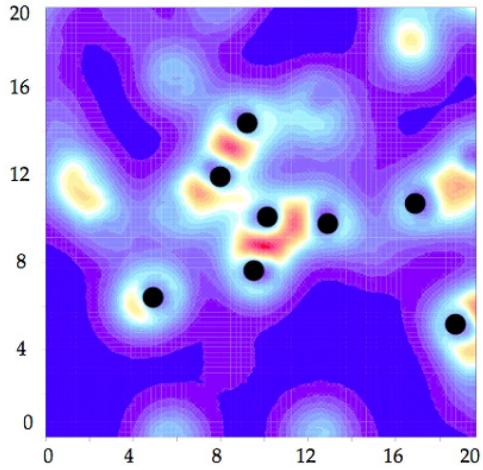

Figure 22. Snapshot of the ion positions in liquid rubidium at $\rho = 0.58$ g cm^{-3} and $T = 1923$ K; ions are full circles and the electron density increases from violet over white to red.

able to reproduce the spectral pattern. This is not unexpected since their approach was based on the nearly free electron model, which is not capable of accurately describing the complex variations in the electronic structure associated with the metal to non-metal transition below $3\rho_{\mathrm{crit}}$. Munejiri and co-workers [8] have also explored the density range of liquid rubidium up to conditions in the vicinity of the liquid–vapour critical point. They tried to obtain the interparticle interactions employing the so called *inverse method*, where very accurate $S(Q)$ data are needed as input. They were also unable to reproduce the experimental $S(Q, \omega)$ pattern shown in figure 20. They attributed this disagreement to the uncertainties in the employed structural data. Another route is chosen in first principle approaches at realistic thermal conditions. The advantage of these methods is that it is no longer necessary to construct potentials for the complex electronic structures in the density regime where electron localization is the dominant effect: *ab initio* calculations on expanded liquid sodium were carried out by Bickham *et al* [92]. They could nicely reproduce the expected drop of the dc conductivity close to the critical point and they also observed aggregation of the Na ions into short living clusters in the low density regime. Alemany *et al* [9] have recently carried out first-principles molecular dynamics studies on liquid rubidium at 1873 K using DFT. As a result they observe the formation of transient aggregates consisting of four to five particles with lifetimes of several vibration periods. The 'terminal' ions of these aggregates are separated by about 10 Å and they perform mutually out-of-phase vibrations with respect to the 'central' ion. Interestingly, a vibration frequency of 3.5 meV is obtained which is in nearly quantitative agreement with the experimental finding from the INS investigations. Similar calculations were recently also preformed by Ross *et al* [10]; however, the calculations were performed with slightly more computational effort, i.e. smaller time steps, larger plane-wave cut off radius and more particles per supercell. Also, the calculations were carried out for several density states between melting and the liquid–vapour critical point, including the experimentally accessed states mentioned above. Similar observations were made as in the aforementioned DFT work. At about twice the critical density, cluster-like structures of four to five ions begin to form, piling up a considerable amount of electronic charge between the constituent rubidium atoms. The lifetime of these aggregates extends over several vibrations. Figure 22 shows as an example

the situation at 1923 K with $\rho = 0.58$ g cm^{-3}. The electron density in the figure is indicated by colours ranging from violet (low density) over white to red (high density).

At the critical point density, however, the simulations clearly indicate the existence of stable rubidium dimers where all the electron density is located between the bonded atoms.

The INS and IXS results on fluid rubidium and caesium together with the computer simulations give a pretty clear picture about the processes that take place in a liquid alkali metal: at sufficiently high density the liquid is clearly monatomic. Below three times the critical density, the screening breaks down and the conductions electrons start to localize. The more duplet states are formed with increasing temperature and decreasing density, a rising tendency is observed to stabilize the electronic structure in localized bonds. Close to ρ_{crit} all the electrons are localized and the system may be represented by a thermal equilibrium between bonded atoms, freely moving ions and thermally ionized particles. The tendency to form singlet states in the expanded fluid may also be viewed as an analogy to a Jahn–Teller effect or a Peierls distortion. Due to the instability of the degenerate states at the Fermi surface, the system transforms into a structurally distorted state, forming localized bonds. The data shown here imply that such a mechanism may in some way participate in the metal to non-metal transition in the fluid alkali metals.

5. The influence of density on the single particle motion

As already mentioned above, inelastic neutron scattering also allows us to obtain information on the individual dynamical properties of the liquid particles from analysing the incoherent scattering law. Experimentally, $S_{\mathrm{incoh}}(Q, \omega)$ can be accessed by different methods: only in very few cases is the nuclear scattering sufficiently incoherent to be directly measured, e.g. in vanadium or in hydrogen dominated samples. If the incoherence results from different spin states of the sample nuclei, coherent and incoherent scattering contributions can generally be separated employing spin polarization techniques which are available at specific scattering instruments, e.g. the D7 spectrometer of the ILL in Grenoble [93]. If on the other hand the incoherency results from the isotopic composition, correspondingly enriched samples need to be used, which however is often extremely costly and therefore in many cases not feasible. If the incoherent contribution is sufficiently large it is also possible to subtract appropriate models for the coherent scattering law. The latter method has been employed in the investigation of liquid sodium [94, 95] where the coherent and incoherent scattering cross sections are of the same order ($\sigma_{\mathrm{coh}} = 1.66$ barn, $\sigma_{\mathrm{incoh}} = 1.62$ barn [96]). At small momentum transfer, the incoherent spectra are narrow with large amplitude but decrease and broaden with rising Q, maintaining their integral value,

$$S_{\mathrm{incoh}}(Q) = \int_{-\infty}^{+\infty} S_{\mathrm{incoh}}(Q, \omega)\, \mathrm{d}\omega = 1. \tag{5.1}$$

However, the coherent contribution is small in the lower Q-range and increases towards the structure factor maximum. Hence, at not too large momentum transfer the incoherent scattering contribution dominates if both cross sections are at least of similar order as is the case for liquid sodium.

According to equation (3.7), the most direct theoretical approach to the incoherent scattering law is possible if adequate models for the self part of the van Hove correlation function $G_{\mathrm{self}}(r, t)$ are available. For two idealized systems such models can easily be constructed: the most simple and most prominent expression for a suitable van Hove function is given by the solution of Fick's second diffusion law, which describes the motion of a Brownian

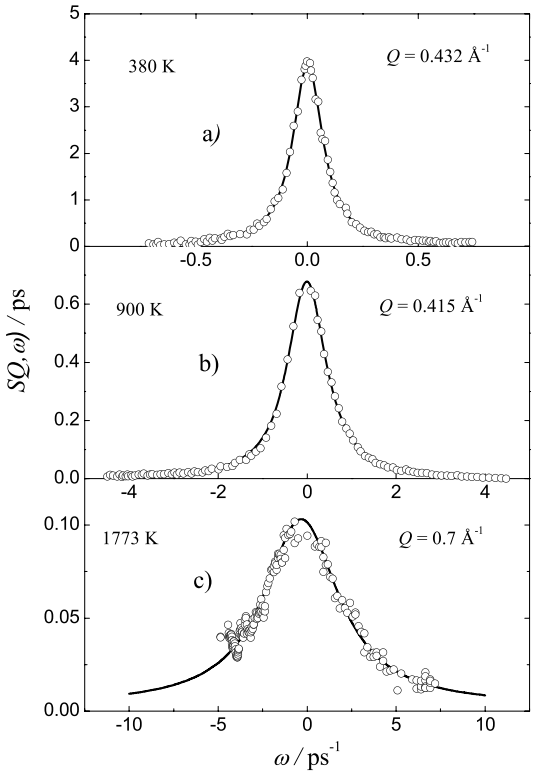

Figure 23. Incoherent scattering spectra for liquid Na at three different temperatures close to the liquid–vapour coexistence curve [95]. Each spectrum corresponds to the lowest attainable Q-value. Open circles are experimental data; solid lines represent Lorentzians fitted to the spectra.

particle in space and time:

$$G_{\mathrm{self}}(r,t) = \frac{1}{(4\pi Dt)^{3/2}} \exp\{-r^2/4Dt\}. \tag{5.2}$$

Here, D is Fick's coefficient of diffusion. The corresponding Fourier transform then reads

$$S_{\mathrm{incoh}}(Q,\omega) = \frac{1}{\pi} \frac{DQ^2}{\omega^2 + (DQ^2)^2}. \tag{5.3}$$

Hence, the scattering law is a simple Lorentzian with halfwidth DQ^2 and the diffusion constant can directly be obtained from experiment. However, it must be kept in mind that Brownian motion is a macroscopically observable process of large and heavy particles, which takes place on long time- and length scales. Thus, the scattering law (5.3) is exactly valid only in the limits $Q \to 0$ and $\omega \to 0$. However, the real limits need not be approached in the experiment to determine the diffusion constant with sufficient accuracy since the scattering law retains its Lorentzian shape up to momentum transfers which are available in ordinary inelastic neutron scattering experiments. This is illustrated in figure 23, where some experimental spectra from an investigation on liquid sodium are shown [95]. The measurements covered a temperature range between melting conditions ($T_{\mathrm{m}} = 371$ K, $\rho_{\mathrm{m}} = 0.98$ g cm^{-3}) and 1773 K ($\rho = 0.58$ g cm^{-3}), where the density is reduced to about 60% of its melting point value, corresponding to about $4\rho_{\mathrm{crit}}$. The spectra in figure 23 represent the lowest Q-values attainable

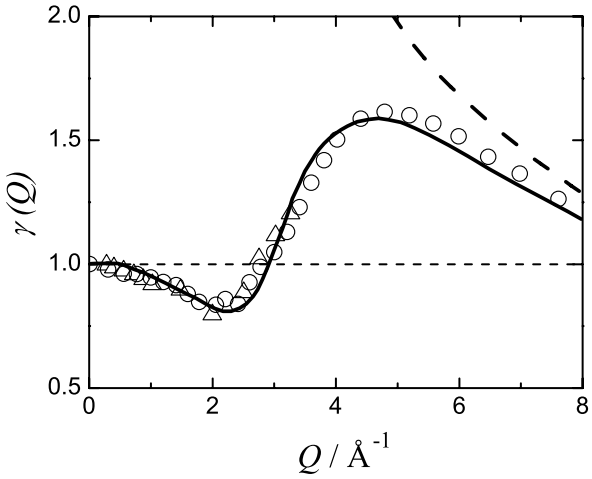

Figure 24. Variation of the reduced halfwidth $\gamma(Q)$ of liquid Na close to melting. Triangles represent experimental data [94, 97], open circles are from MD-simulation [98] and the solid line is the result of a kinetic theory [99]. The long dashed line gives the free particle behaviour of $\gamma(Q)$.

in the respective experiments. Spectra are shown for different temperature/density states along the liquid–vapour coexistence curve between melting and 1773 K (see also figure 3).

A useful quantity to characterize the progressive deviation from the Lorentzian line shape with rising Q is the so called *reduced halfwidth* $\gamma(Q)$, which is defined as the ratio of the experimental halfwidth to the expected value for Brownian motion:

$$\gamma(Q) = \frac{\omega_{1/2}(Q)}{DQ^2} \tag{5.4}$$

The continuous departure from $\gamma(Q) = 1$ with increasing momentum transfer is hence a measure of the progressive deviation of the real diffusion dynamics from the simple Brownian picture if decreasing time- and length scales are probed with rising Q. In most cases $\gamma(Q)$ decreases with momentum transfer if Q is not too high, i.e. the real halfwidth broadens more slowly than predicted by (5.3). However, the complete Q-dependence is more complex and a rather oscillatory behaviour is found, which is depicted in figure 24 for a wider Q-range. Data shown are taken from experiment [94, 97], from MD-simulation [98] and also from a mode coupling approach [99].

At the other extreme, at large Q and large ω the probed time- and length scales are too small for the particles to interact and $G_{\mathrm{self}}(r, t)$ can be approximated by the behaviour of free particles. The trajectories of such particles are linear and their momenta obey a Maxwellian distribution. An averaging in momentum space then gives [35, 36]

$$G_{\mathrm{self}}(r, t) = \left(\frac{M}{2\pi k_{\mathrm{B}} T t^2}\right)^{3/2} \exp\left\{-\frac{Mr^2}{2k_{\mathrm{B}} T t^2}\right\}, \tag{5.5}$$

with Fourier transform

$$S_{\mathrm{incoh}}(Q, \omega) = \left(\frac{M}{2\pi k_{\mathrm{B}} T Q^2}\right)^{1/2} \exp\left\{-\frac{M\omega^2}{2k_{\mathrm{B}} T Q^2}\right\}. \tag{5.6}$$

I.e., in that limit the scattering law comprises a Gaussian shape in ω. It is easily shown that the reduced halfwidth is now $\propto 1/Q$. It is also given in figure 24 as the long dashed line.

Apparently, the scattering law transforms from a Lorentzian line shape in the $Q \to 0$ limit to a Gaussian behaviour at sufficiently large momentum transfer. However, the exact

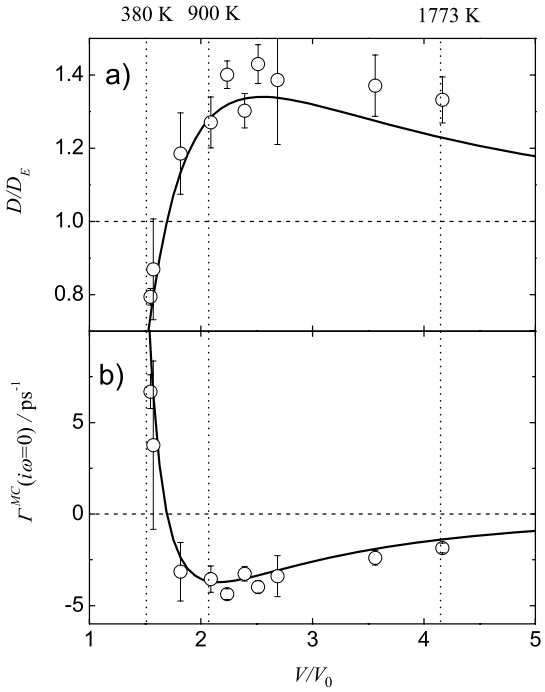

Figure 25. (a) Reduced diffusion coefficient D/D_{E} versus reduced volume $V/V_0 = \sqrt{2}/n\sigma^3$. (b) Density dependence of the mode-coupling contribution $\tilde{\Gamma}^{\mathrm{MC}}$ versus reduced volume. Circles are experimental data on Na, the solid line represents the hard-sphere result [102], and dotted lines give corresponding temperatures for states close to the vapour pressure line in liquid sodium.

$S_{\mathrm{incoh}}(Q,\omega)$ in the intermediate region which connects the two limits is unknown. Models for this range where the short range interactions between the particles determine the motional behaviour and where $\gamma(Q)$ increases towards the free particle limit are much more difficult to obtain.

The easiest theoretical approach to an understanding of the diffusive motion in liquids is the Enskog model [100], which assumes that the particles behave like hard spheres interacting solely through binary collisions. The diffusion coefficient is then given by

$$D_{\mathrm{E}} = \frac{1}{16}\sqrt{\frac{\pi k_{\mathrm{B}} T}{M}}\frac{\sigma}{\eta g(\sigma)}. \tag{5.7}$$

σ is the hard sphere diameter of the particles and $g(\sigma) = (1-\eta/2)/(1-\eta)^3$ is the pair correlation function related to the packing fraction $\eta = \pi n\sigma^3/6$, with n being the number density. The advantage of equation (5.7) is that the density dependence of the diffusion coefficient is easily computed if corresponding values for the hard sphere diameter are available [67]. However, MD simulations on simple hard sphere systems [61, 101] show that the diffusional dynamics is considerably more complicated as predicted by (5.7). The real particle dynamics of the hard spheres is controlled by complex correlations and collisions where more than just two particles are involved. The microscopic processes ruling the particle motion are also found to depend characteristically on density. This is illustrated in figure 25(a), where the ratio of the diffusion constant normalized to the corresponding Enskog value is given as a function of liquid volume per particle, scaled to close packing volume $V_0 = n\sigma^3/\sqrt{2}$.

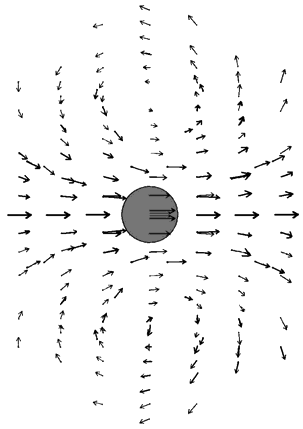

Figure 26. Formation of a vortex pattern in the velocity field around a diffusing particle at intermediate density as obtained from a hard sphere MD simulation and from a hydrodynamic model (after [61]). The arrows represent the velocity field around the particle (grey sphere, moving from left to right).

If Enskog theory applied D/D_E should be equal to one for all volumes (dashed line); however, figure 25 shows that the real diffusion coefficient deviates considerably from this prediction. The solid line represents results from a computer generated hard sphere system [102]; the open circles are obtained from the aforementioned neutron scattering investigations on liquid sodium [95]. The agreement between simulation and experiment is excellent, indicating that the diffusion dynamics in liquid sodium can be nicely approximated to be hard sphere fluid-like, at least along the temperature/density range investigated so far. At high density, close to melting, the forward motion is considerably hindered, while at slightly reduced density, corresponding to boiling conditions, processes set in which support the translational motion of the diffusing particle. On a purely qualitative basis this behaviour can already be understood: at high density the free diffusion is hindered by a more or less rigid sphere of next neighbours surrounding the particle under consideration. This is the so called cage effect, which introduces a negative contribution into the velocity autocorrelation function also in a pure hard sphere system. On the other hand, at lower density an examination of the particle trajectories from computer simulation studies [61] reveals that a diffusing atom generates a vortex pattern of the velocity field in its immediate vicinity which couples to its translational motion and adds an additional contribution to the particle diffusion (see figure 26).

5.1. Theoretical aspects

In order to put the understanding of the density dependence of the diffusion coefficient on a more quantitative basis it is necessary to go one step deeper into the theoretical framework of microscopic single particle dynamics.

The diffusion of a tagged particle is determined by the *velocity auto-correlation function* (VACF), which is characteristic for each system and defined as

$$\Phi(t) = \frac{\langle \vec{v}_i(0) \cdot \vec{v}_i(t) \rangle}{\langle \vec{v}_i(0) \rangle^2}. \tag{5.8}$$

Here, $\vec{v}_i$ is the velocity vector of particle i and the brackets again denote an ensemble average. This function can directly be obtained from computer simulations, since there the positions

and momenta of all particles are known at all times and the ensemble averaging can easily be performed. In an experiment, however, one measures the macroscopic diffusion coefficient D which is related to the integral value of the VACF [103]:

$$D = \frac{k_B T}{M} \int_0^\infty \Phi(t)\,\mathrm{d}t. \tag{5.9}$$

In analogy to equation (4.4), the VACF can be obtained from solving a corresponding generalized Langevin equation

$$\dot{\Phi}(t) = -\int_0^\infty \Gamma(t-t')\Phi(t')\,\mathrm{d}t', \tag{5.10}$$

where $\Gamma(t)$ now represents the memory function of the velocity autocorrelation. However, the drawback of equation (5.10) is once more that the memory function $\Gamma(t)$ of the VACF is *a priori* not known, which is again the key problem to understand the single particle motion. Although we saw above that the microscopic motional dynamics is unquestionably much more complicated than predicted by the simple two particle collision theories, it is known from computer simulations that the main contribution to the memory function still comes from these processes. This contribution is given by a simple Gaussian decay in time [103]:

$$\Gamma(t)_B = \omega_E^2 \mathrm{e}^{-t^2/\tau^2}. \tag{5.11}$$

ω_E^2 is the Einstein frequency defined in equation (3.19) and τ is the characteristic time constant for binary collisions. It is usually of the order of a tenth of the Enskog time [36].

We can interpret the integral in equation (5.9) as the Laplace transform of the VACF at $z = \mathrm{i}\omega = 0$:

$$\tilde{\Phi}(z=0) = \left[\int_0^\infty \Phi(t)\mathrm{e}^{zt}\,\mathrm{d}t\right]_{z=0} = \int_0^\infty \Phi(t)\,\mathrm{d}t. \tag{5.12}$$

Also, in Laplace subspace, the generalized Langevin equation (5.10) reads

$$\tilde{\Phi}(z) = \frac{1}{z + \tilde{\Gamma}(z)}. \tag{5.13}$$

Combining equations (5.9), (5.12) and (5.13) gives

$$D = \frac{k_B T/M}{\tilde{\Gamma}(z=0)}, \tag{5.14}$$

which correlates the memory function of the velocity autocorrelation directly with the experimentally accessible diffusion constant. The expression resembles the well known Einstein relation for Brownian motion, which relates the diffusion coefficient to the macroscopic friction coefficient of the liquid in the same way. If the Laplace transform of equation (5.11) were used in equation (5.14) the Enskog diffusion coefficient would again be obtained. However, as we saw earlier, the real diffusion constant of a simple liquid deviates from the Enskog prediction and the computer simulations suggest that more complicated correlations are also involved. These further correlations are taken into account by an additional term to the memory function:

$$\Gamma(t) = \Gamma_B(t) + \Gamma_{MC}(t). \tag{5.15}$$

While $\Gamma_B(t)$ determines the particle's behaviour on very short times due to binary collisions, $\Gamma_{MC}(t)$ rules the motion on longer timescales. The exact form of this additional term can again be obtained from computer simulations but for some examples it was also established within the framework of *mode coupling theory* (MCT). The problem of these approaches however—at least from the viewpoint of neutron scattering—is that MCT does usually not provide a direct access to the scattering law. On the other hand, other quantities which are accessible from experiment may be available, for instance the diffusion coefficient D and also the reduced halfwidth $\gamma(Q)$.

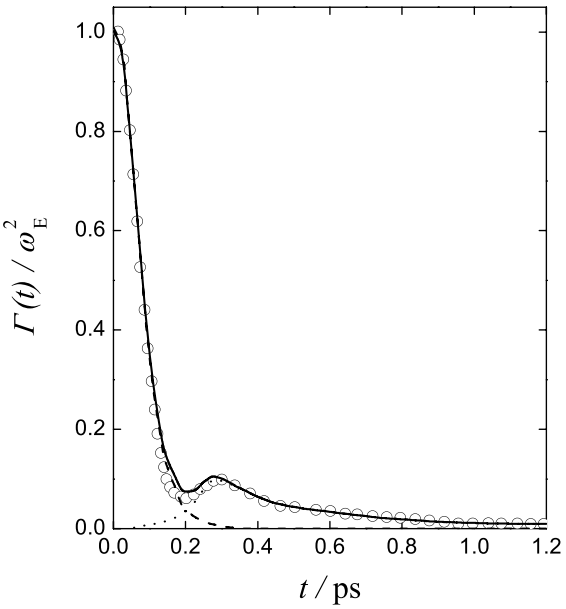

Figure 27. Memory function of the VACF $\Gamma(t)$ of liquid Na close to melting: O, computer simulation; – – –, short time contribution $\Gamma_B(t)$; · · ·, MCT contribution $\Gamma_{MC}(t)$ (equation (5.16)); —, $\Gamma_B(t) + \Gamma_{MC}(t)$.

5.2. Microscopic diffusion at high density

As already indicated above, the computer simulations show that $\Gamma(t)$ decays considerably slower than predicted by equation (5.11). Theoretically, this 'long-time behaviour' is accounted for in the additional term $\Gamma_{MC}(t)$ appearing in equation (5.15). It was suggested by Balucani and co-workers [104] that at high density the main contribution to this term stems from a coupling between collective density fluctuations and the diffusive motion. In order to account for the reduced diffusion constant compared to D_E it was furthermore suggested to couple the forward motion specifically to the slow oscillation modes which appear with wavevector Q_0 (minimum in the dispersion relation, also see figure 6). As a side-effect, this also leads to a considerable simplification of the theoretical formalism and the following form for the memory function is obtained:

$$\Gamma(t) = \omega_E^2 e^{-t/\tau} + \frac{k_B T}{6nM\pi^2} \frac{A}{S(Q_0)} [F_S(Q_0, t) - F_0(Q_0, t)] F(Q_0, t). \qquad (5.16)$$

In equation (5.16), $F_S(Q_0, t)$ and $F_0(Q_0, t)$ are respectively the intermediate scattering functions of the single particle motion and the well known free particle limit, $F(Q_0, t)$ is the intermediate scattering law containing the collective modes. Q_0 denotes the position of the main maximum in $S(Q)$. The constant A represents the integral over the correlation function $h(Q) = S(Q) - 1$. The validity of this approach was demonstrated in comparing $\Gamma(t)$ obtained from equation (5.16), employing the models in equations (5.3), (5.6) and (4.7) to compute the intermediate scattering functions, with the direct result of an MD simulation [98] on liquid sodium close to melting where the potential in equation (1.2) has been used. A nearly quantitative agreement between the two functions was found, which is shown in figure 27. At small times $\Gamma(t)$ decays according to equation (5.11), while at larger times the additional contribution due to equation (5.15) becomes visible. This is clear evidence for the coupling to collective longitudinal modes which is responsible for the extension of the memory

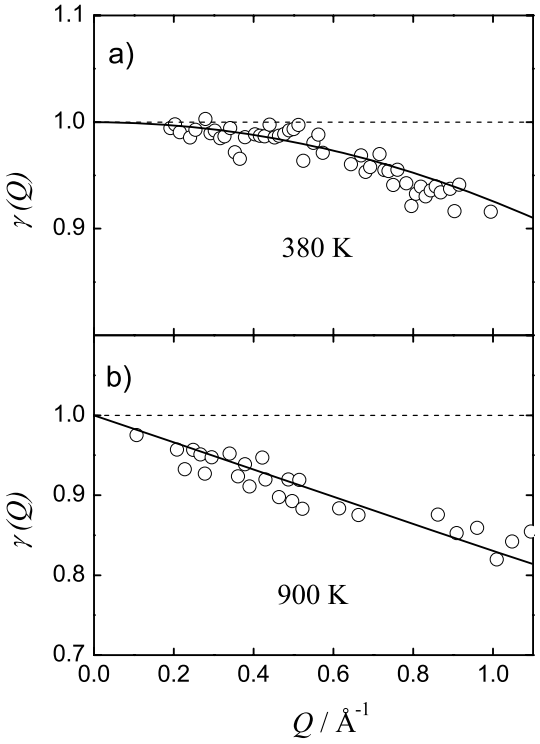

Figure 28. Reduced halfwidth $\gamma(Q) = \omega_{1/2}^{\exp}/DQ^2$ for Na at (a) 380 K and at (b) 900 K. Solid lines are MCT results [104, 106]; open circles represent experimental data [95, 97].

function to longer times. Of course, this additional contribution also appears in the Laplace transform of equation (5.16) and hence causes a decrease of the diffusion coefficient D due to equation (5.14).

From the simulation the diffusion coefficient can quantitatively be obtained and a value of $D_{\mathrm{MD}} = 0.426 \times 10^{-4}$ cm^2 s^{-1} is found, which is in perfect agreement with the value obtained from the neutron experiment ($D_{\exp} = 0.423 \times 10^{-4}$ cm^2 s^{-1}). Furthermore, both values are in good accord with the literature value from Meyer and Nachtrieb ($D_{\mathrm{Lit}} = 0.406 \times 10^{-4}$ cm^2 s^{-1}), obtained using the capillary reservoir technique [105].

Additionally, the theoretical approach also allows a prediction of the reduced halfwidth $\gamma(Q)$ and a quadratic deviation from $\gamma(Q) = 1$ is obtained:

$$\gamma(Q) = 1 - c(n,T)Q^2; \qquad c(n,T) = 0.074\ \text{Å}^2. \tag{5.17}$$

This behaviour is also in quantitative agreement with the experimental observation as can be inferred from figure 28.

The coupling to longitudinal collective modes seems to be essential in describing the exact diffusional behaviour at high density: the tagged particle oscillates with frequency ω_{E} in the cage of next neighbours, resulting in a contribution to the memory function which is given by (5.11). However, the actual forward motion is accomplished by coupling to a longitudinal collective mode which carries the particle together with its immediate surroundings from one place to the other. It is interesting to note that the situation is similar to the description of the collective dynamics where two processes were also needed for an adequate memory function to model the density–density correlation.

5.3. Self-diffusion at intermediate density

At 900 K and slightly decreased density, at a state which corresponds to the boiling conditions of liquid sodium, the processes ruling the diffusive motion seem characteristically to change as is inferred by figure 25(a). The coupling to longitudinal modes seems no longer to be appropriate. Instead it has been proposed to assume a coupling to transverse modes. This view is motivated by the findings from an older computer simulation carried out by Alder and Wainwright about 30 years ago [61] where the formation of a vortex pattern around the diffusing particle has been observed as is illustrated in figure 26, which was taken from this work.

The coupling to transverse modes was additionally considered in an MCT ansatz by Wahnström and Sjögren [106]. An explicit $S_{\mathrm{incoh}}(Q,\omega)$-model has been developed by de Schepper and Ernst [107] taking into account only transverse fluctuations. Theoretically, the scattering law can then be obtained from the generalized Langevin formalism employed on the intermediate scattering function:

$$\dot{F}_{\mathrm{S}}(Q,t) = -\int_0^\infty M(Q,t') \cdot F_{\mathrm{S}}(Q,t-t')\,\mathrm{d}t' \tag{5.18}$$

which in Laplace subspace reads

$$\tilde{F}_{\mathrm{S}}(Q,z) = \frac{1}{z+\tilde{M}(Q,z)}. \tag{5.19}$$

As an ansatz to solve equation (5.18) a Q- and z-dependent diffusion constant was introduced in imitation of the hydrodynamic picture to express the corresponding memory function:

$$\tilde{M}(Q,z) = Q^2 D(Q,z). \tag{5.20}$$

This results in a simple form for the scattering law:

$$S_{\mathrm{incoh}}(Q,\omega) = \frac{1}{\pi}\,\mathrm{Re}\left(\frac{1}{z+Q^2 D(Q,z)}\right). \tag{5.21}$$

Instead of making assumptions for a passable memory function, the problem is now to find an adequate diffusion coefficient $D(Q,z)$ in order to calculate the appropriate scattering law. However, it is assumed that this quantity is given by the classical value of the diffusion coefficient D_{E} plus an additional term $\delta U(Q,z)$ which contains the required modification to match the experimentally observed value [107]:

$$D(Q,z) = D_{\mathrm{E}} + \delta U(Q,z). \tag{5.22}$$

$\delta U(Q,z)$ is then calculated in the framework of mode coupling theory, where however only coupling to transverse modes are regarded. Although the exact derivation of this term is highly sophisticated, the theory finally allows us to quantitatively calculate the diffusion coefficient D and again the behaviour of the reduced halfwidth $\gamma(Q)$ in the lower momentum transfer range. For liquid sodium at 900 K a diffusion coefficient of $D_{\mathrm{MC}} = 0.217 \times 10^{-4}$ cm^2 s^{-1} is obtained from this approach, which is again in good accord with the experimental neutron result of $D_{\mathrm{exp}} = 0.298 \times 10^{-4}$ cm^2 s^{-1} at the same temperature [95]. The deviation of the reduced halfwidth from $\gamma(Q) = 1$ is now found to be linear:

$$\gamma(Q) = 1 - bQ, \tag{5.23}$$

and for b, theory predicts a value of $b = 0.16$ Å. Again, a nearly perfect agreement between experiment and theory exists as can be seen from figure 28(b).

Again, the excellent agreement between experiment and theory shows that the microscopic processes ruling the diffusive dynamics are far from simple binary collision behaviour. Instead,

coupling to transverse modes explains the diffusion quantitatively. It should also be noted that this view is complementary to the MD observation of a vortex pattern in the velocity field around a diffusing hard sphere which also supports forward motion (see figure 26). This coupling is now an additional process which becomes important mainly for the diffusive motion of the single particle, while for the collective dynamics no characteristic variations in the distinct motional behaviour is observed at these thermodynamic conditions.

5.4. The low density liquid

Figure 25(a) shows that with decreasing density (increasing volume) the reduced diffusion coefficients of both experiment and computer simulation gradually return towards the predicted Enskog value. Apparently, with decreasing density, mode coupling contributions cease to exist and the dynamics is progressively determined by simple binary collisions. Using equation (5.15) in equation (5.14) the diffusion coefficient can be expressed in the following way:

$$\begin{aligned} \frac{1}{D_{\mathrm{exp}}} &= \frac{\tilde{\Gamma}_{\mathrm{B}}}{k_{\mathrm{B}}T/M} + \frac{\tilde{\Gamma}_{\mathrm{MC}}}{k_{\mathrm{B}}T/M} \\ \Rightarrow \tilde{\Gamma}_{\mathrm{MC}} &= \frac{k_{\mathrm{B}}T/M}{D_{\mathrm{exp}}}\left(1 - \frac{D_{\mathrm{exp}}}{D_{\mathrm{B}}}\right). \end{aligned} \tag{5.24}$$

Identifying D_{B} with D_{E} we can now calculate the volume dependence of the mode coupling contribution. This is shown in figure 25(b). At high density, the mode coupling term is large and positive, causing the real diffusion coefficient to decrease below the classical Enskog value. At $V/V_0 \approx 1.4$, $\tilde{\Gamma}_{\mathrm{MC}}$ becomes negative, i.e. $D_{\mathrm{exp}} > D_{\mathrm{B}}$. At very high temperature and correspondingly large volumes the mode coupling contribution decreases and finally ceases to exist. However, extrapolating the full line in figure 25(b) until it matches the Enskog value ($D/D_{\mathrm{E}} = 1$), i.e. where the dynamics is solely determined by binary collisions, conditions are reached which no longer correspond to the liquid state of sodium.

Generally, one can say that the actual value of the macroscopic diffusion constant is ruled by microscopic processes which can be identified as a coupling of the diffusive mode to collective excitations. The exact mechanism depends on density. In the dense melt, the main contribution comes from a coupling to longitudinal fluctuations which are mainly responsible for the overall forward motion of the particle. A slight reduction of the density suffices for a second mechanism, a coupling to transverse density fluctuations, to now becomedominant, leading to an enhancement of the mean propagation speed. The coupling mechanisms are however only effective at sufficiently large density. With increasing volume the coupling disappears and the dynamics is gradually determined by simple binary collisions.

6. Conclusion and perspective

With the presentation of the above given data we have tried to give a comprehensive view of the dynamic properties of the fluid alkali metals in order to characterize the microscopic particle motion along the full density range between melting and the liquid–vapour critical point. One of the most striking particularities of this group of liquids is the distinct ability to sustain collective modes down to wavelengths on the atomic scale. Although this ability is nowadays known to be a general feature of all liquids and specifically of liquid metals, the collective dynamics in the molten alkali metals is especially pronounced. In no other liquid do the collective excitations appear as such distinct peaks in the scattering law and extend to such high Q-values. One explanation for this has already been given in section 4, bringing up the influence of the C_P/C_V ratio in these systems. However, this is just a phenomenological observation and does not lead

to an understanding of the underlying physics. As already mentioned in the introduction, the origin of this property is rather related to the specific interatomic interactions in the alkali metals. They differ considerably from those in other liquids and also from those in other liquid metals. Alkali metals are perfect model systems to be treated within the view of free and nearly free electron theories. This means that the electron system can adequately be described using bare Coulomb potentials screened by relatively simple functions. This view also leads to the well known characteristic shape of the pseudo-potentials, with their distinct oscillatory behaviour with rising distance. It is tempting to also relate the particular particle dynamics in liquid alkali metals to simple free electron systems. In fact, such approaches have been known for a long time, e.g. the acquainted Bohm–Staver model [108], where the dielectric function of the electron gas determines the ionic fluctuations in the lower Q-range. The predictions of this model were recently compared to INS results on molten potassium [109] and molten alkali metal alloys [110]. Some qualitative agreement was found; however, a quantitative conformity leading to a generalized understanding of the collective dynamics in molten alkali metals was not observed. Nevertheless, the data presented here show that the specific nature of the particle motion remains unchanged as long as the density is not reduced to below a specific value at which considerable variations are also observed in the magnetic and electronic properties, indicating the breakdown of the delocalized electron system. Up to these conditions of temperature and pressure the dynamical features are obviously determined by the same kind of forces, resulting from the metallic binding between the particles.

In the investigation of the diffusional properties in liquid sodium the thermodynamic conditions necessary to enforce the radical variation of the interparticle interactions due to the breakdown of the metallic regime were not reached. Therefore it was only possible to describe the single particle motion in liquid sodium in analogy to a computer generated model system of hard spheres over wide density ranges, because there the metal to non-metal transition was certainly not taken into account, too. The same observation was made for the collective dynamics, where the general features remain more or less unchanged, only the relevant relaxation mechanisms become faster due to the increasing temperatures, leading to an overall broadening in $S(Q, \omega)$ (section 4.3).

Principal changes in the dynamics are finally observed when the screening breaks down and the electrons settle at their parent ions (section 4.4). The susceptibility then shows a distinct rise, indicating the increasing number of local magnetic moments. However, the rising number of identical spin $1/2$ states then leads to another instability and the system tends to minimize its energy by spin pairing and finally by formations of molecular units. With further decreasing density the dissociation energy of these units increases, indicative of the rising stability of these particles. At sufficiently reduced density stable molecules are formed which in the gas phase can be identified employing methods of optical spectroscopy.

The fluid alkali metals are a highly interesting system showing a rich variety of physical phenomena which are not yet understood on a quantitative basis. The continuous 'chemical' transformation with varying density is still not fully unravelled and a lot still needs to be done.

There is also much to do in order to fully comprehend liquid dynamics on the microscopic scale in general. However, the current technological progress raises hope to solve many of the longstanding questions in the near future: computer simulations become more and more realistic due to the rapid increase in computing power allowing us to use larger and more realistic particle numbers in MD simulations. Also, *ab initio* methods become more and more reliable.

The situation is similar on the experimental side: the quality of the currently available neutron and x-ray data has considerably improved due to many technological developments over the last 10 years and the progress is still continuing. One example is the advent of the new

third generation synchrotron over the last ten years. Promising hope is also set on new radiation sources, e.g. the modern powerful spallation facilities which are currently being installed as e.g. the second target station at ISIS in the UK, the SNS in the USA or the new J-PARC neutron source in Japan. A lot of expectations are also focused onto the new free electron x-ray sources which are currently being developed and which are expected to be available within a few years. The prospect to use faster computers and new experimental radiation sources in the near future is highly motivating, and perhaps some of the still standing questions in liquid dynamics may then be solved. Through this review we tried to emphasize that an exact understanding of the particle behaviour in liquids on the microscopic time- and length scale is still lacking and that our current knowledge is based primarily on phenomenological considerations. Whilst the physical picture appears to be quite clear in the hydrodynamic regime, where the characteristic features of the scattering law are understood by means of the macroscopic transport coefficients, many questions are left open in the domain where general hydrodynamics applies. Some still open questions concern the accessibility of the transition Q-range from the hydrodynamic to the generalized hydrodynamics regime. E.g., as already mentioned in section 4.3, an intermediate Q-range may exist where the propagation speed of the collective modes changes from adiabatic to isothermal before approaching the momentum transfer region where the so called anomalous dispersion sets in (see section 4.4). For many liquids this Q-range can be estimated to lie at or below about 0.1 Å^{-1}. It is therefore hardly accessible in conventional x-ray or neutron experiments and there is hence no clear evidence for its existence although weak experimental indications obtained from a neutron investigation on molten Ni exist [111]. This metal is particularly interesting in this respect because it comprises a relatively large value for γ, the ratio of the heat capacities. Hence, the transition from the adiabatic to the isothermal mode propagation should be clearly distinguishable in this liquid metal. Although the investigation of this system is not easy due to the high melting temperature and the still existing problems in accessing the appropriate Q-range, it is worth exploring in more detail because a fundamental physical question is addressed here.

The accessibility of this Q-range would also allow exploring the detailed bending up of the dispersion relation due to the increase of the mode velocity towards c_∞ with rising Q and ω. A possible explanation for this effect was given in section 4.4 within the framework of extended hydrodynamics, where the rise of the propagation speed for the longitudinal modes was related to the onset of shear forces at high frequencies. This view seems to be appropriate for the liquid alkali metals; however, in other liquid systems the same explanation is not so unambiguous. This is e.g. the case in molten ionic liquids, where the theoretically predicted shear modulus [112] differs considerably from the experimental observation [113]. It must also be emphasized that positive dispersions similar to those in liquids are also a well known feature in glasses, which somewhat questions the interpretation of this effect in terms of a transition from liquid-like to solid-like at sufficiently high frequency.

One big disadvantage of generalized hydrodynamics is its purely phenomenological character and accordingly the memory functions are introduced. Exponential decays as used to approximate many functions are only used to maintain simplicity in order to get the Q-dependence of many dynamic quantities. The same is certainly true for the time constants in the one- and two-relaxation-time models described here. However, the physical meaning of these time constants remains nebulous and is still subject to speculation. From the viewpoint of an experimentalist it would be highly preferable if theory tried to develop clear models for memory functions which could directly be tested in comparison to experiment. Mode coupling theory provides such a description on a clearer physical background (see e.g. [114]); however, the theoretical framework often appears to be too bulky to be employed for the direct analysis of experimental data.

Another important aspect in the attempt to comprehend liquid dynamics is the question of the thermodynamic state. As mentioned in section 2.1, the liquid state extends over wide ranges of the thermodynamic variables. However, liquid dynamics is usually explored only in the dense phase close to melting. Only a few examples exist where investigations were extended along the full liquid state (see e.g. [1] and references therein). The main reason for this deficiency is that often high temperatures and simultaneously applied high pressures are needed, which make such experiments a very difficult task. Nevertheless, it would be preferable if inelastic scattering experiments were extended over the full density range of the liquid state. This could lead to highly interesting results, especially in those systems where density is not the only order parameter, but where state dependent variations in molecular structure and/or the interparticle interactions are expected [1, 115]. For this, however, it would be necessary to develop new and powerful sample environments capable of running for several days even under extreme conditions of temperature and pressure. For other experimenting techniques such experimental set-ups exist (see e.g. [116]) and it would be highly interesting to also adopt these techniques for their use in neutron- and x-ray scattering experiments.

Acknowledgments

The authors would like to thank the local contacts and staff at the ESRF and the ILL in Grenoble, France, and acknowledge the great experimenting conditions at both facilities. We are also grateful for financial support by the Bundesministerium für Bildung und Forschung (BMBF).

References

[1] Hensel F and Warren W W 1999 *Fluid Metals* (Princeton, NJ: Princeton Press)
[2] Price D L, Singwi K S and Tosi M P 1970 *Phys. Rev.* B **2** 2983
[3] Ashcroft N W 1966 *Phys. Lett.* **23** 48
[4] Singwi K S, Sjölander A, Tosi M P and Land R H 1970 *Phys. Rev.* B **1** 1044
[5] Balucani U, Torcini A and Valauri R 1993 *Phys. Rev.* B **47** 3011
[6] Cannales M and Padro J A 1997 *Phys. Rev.* E **56** 1759
Cannales M and Padro J A 1999 *Phys. Rev.* E **60** 551
Anento N, Padro J A and Cannales M 1999 *J. Chem. Phys.* **111** 10210
[7] Pilgrim W-C, Winter R and Hensel F 1993 *J. Phys.: Condens. Matter* **5** B183
[8] Munejiri S, Shimojo F and Hoshino K 2000 *J. Phys.: Condens. Matter* **12** 4313
[9] Alemany M M G, Martins J L and Cabral B J 2004 *J. Non-Cryst. Solids* **347** 100
[10] Ross M, Yang L H and Pilgrim W-C 2006 *Phys. Rev.* B at press
[11] Redmer R and Warren W W 1993 *Phys. Rev.* B **48** 14892
[12] Huiben M J and van der Lugt W 1979 *Acta Crystallogr.* A **35** 421
[13] van der Lugt W and Alblas B P 1985 *Handbook of Thermodynamic and Transport Properties of the Alkali Metals* ed R Ohse (Oxford: Blackwell Scientific Publications) p 299
[14] Hensel F, Hohl G F, Schaumlöffel D and Pilgrim W-C 2000 *Z. Phys. Chem.* **214** 823
[15] Ohse R W, Babelot J-F, Magill J and Tetenbaum M 1985 *Handbook of Thermodynamic and Transport Properties of the Alkali Metals* ed R Ohse (Oxford: Blackwell Scientific Publications) p 329
[16] Pilgrim W-C, Winter R, Hensel F, Morkel C and Gläser W 1991 *Ber. Bunsenges. Phys. Chem.* **95** 1133
[17] Hosokawa S and Pilgrim W-C 2001 *Rev. Sci. Instrum.* **72** 1721
[18] Dorner B and Peisl H 1983 *Nucl. Instrum. Methods* **208** 587
[19] Burkel E 1992 *Inelastic Scattering of X-rays with Very High Energy Resolution* (Berlin: Springer)
[20] Sette F, Ruocco G, Krisch M, Bergmann U, Masciovecchio C, Mazzacurati V, Signorelli G and Verbeni R 1995 *Phys. Rev. Lett.* **75** 850
[21] Masciovecchio C *et al* 1996 *Nucl. Instrum. Methods* B **111** 181
[22] Sinn H *et al* 2001 *Nucl. Instrum. Methods* **467/468** 617

[23] Baron A, Tanaka Y, Miwa D, Ishikawa D, Mochizuki T, Takeshita K, Goto S, Matushita T and Ishikawa T 2001 *Nucl. Instrum. Methods* **467/468** 627
[24] Randolph P D 1963 *Phys. Lett.* **3** 162
[25] Randolph P D 1964 *Phys. Rev.* **134** A1238
[26] Kinell T *et al* 1985 *J. Phys. F: Met. Phys.* **15** 1033
[27] Sinn H, Sette F, Bergmann U, Halcousis Ch, Krisch M, Verbeni R and Burkel E 1997 *Phys. Rev. Lett.* **78** 1715
[28] Pilgrim W-C, Hosokawa S, Saggau H, Sinn H and Burkel E 1999 *J. Non-Cryst. Solids* **250–252** 96
[29] Copley J R D and Rowe J M 1974 *Phys. Rev. Lett.* **32** 49
[30] Aisa D *et al* 2005 *Not. Neutroni e Luce di Sincrotrone* **10** 20
[31] http://www.isis.rl.ac.uk/molecularspectroscopy/iris/
[32] http://www.isis.rl.ac.uk/excitations/mari/
[33] http://www.esrf.fr/UsersAndScience/Experiments/HRRS/ID16/
[34] Egelstaff P A 1994 *An Introduction to the Liquid State* (*Oxford Series on Neutron scattering in Condensed Matter*) 2nd edn (Oxford: Clarendon)
[35] Balucani U and Zoppi M 1994 *Dynamics of the Liquid State* (*Oxford Series on Neutron scattering in Condensed Matter*) (Oxford: Clarendon)
[36] Boon J P and Yip S 1980 *Molecular Hydrodynamics* (New York: Dover)
[37] Lovesey S W 1986 *Theory of Neutron Scattering from Condensed Matter* (Oxford: Oxford University Press)
[38] Verkerk P 2001 *J. Phys.: Condens. Matter* **13** 7775
[39] Copley J R D and Lovesey S W 1975 *Rep. Prog. Phys.* **38** 461
[40] Schülke W 1991 *Inelastic Scattering by Electronic Excitations* (*Handbook of Synchrotron Radiation*) vol 3, ed G Brown and D E Moncton (Amsterdam: Elsevier Science)
[41] Burkel E 1991 *Inelastic Scattering of X-rays with Very High Energy Resolution* (Berlin: Springer)
[42] van Hove L 1954 *Phys. Rev.* **95** 249
[43] Hubbard J and Beeby J L 1969 *J. Phys. C: Solid State Phys.* **2** 556
[44] Levesque D, Verlet L and Kürkijarvi J 1973 *Phys. Rev.* A **7** 1690
[45] Rahman A 1974 *Phys. Rev.* A **9** 1667
[46] Mezei F 1972 *Z. Phys.* **255** 146
[47] Mountain R D 1966 *Rev. Mod. Phys.* **38** 205
[48] Kardanoff L P and Martin P C 1963 *Ann. Phys.* **24** 419
[49] Landau L and Placzek G 1934 *Phys. Z. Sowj.* **5** 172
[50] Beyer R T 1985 *Handbook of Thermodynamic and Transport Properties of the Alkali Metals* ed R Ohse (Oxford: Blackwell Scientific Publications) p 525
[51] Cook J G and Fritsch G H 1985 *Handbook of Thermodynamic and Transport Properties of the Alkali Metals* ed R Ohse (Oxford: Blackwell Scientific Publications) p 735
[52] Scopigno T, Ruocco G and Sette F 2005 *Rev. Mod. Phys.* **77** 881
[53] Berne B J and Pecora R 1976 *Dynamic Light Scattering* (New York: Wiley–Interscience)
[54] Fåk B and Dorner B 1992 *Report No.* 92FA008S, Institute Laue Langevin
[55] Shimojo F, Hoshino K and Watabe M 1994 *J. Phys. Soc. Japan* **63** 141
[56] Hasegawa M, Hoshino K, Watabe M and Young W H 1990 *J. Non-Cryst. Solids* **117/118** 300
[57] Ichimaru S and Utsumi K 1981 *Phys. Rev.* B **24** 7385
[58] Zwanzig R 1960 *J. Chem. Phys.* **33** 1338
[59] Lovesey S W 1971 *J. Phys. C: Solid State Phys.* **4** 3057
[60] Waseda Y 1980 *The Structure of Noncrystalline Materials; Liquids and Amorphous Solids* (New York: McGraw-Hill)
[61] Alder B J and Wainwright T E 1970 *Phys. Rev.* A **1** 18
[62] Scopigno T, Balucani U, Ruocco G and Sette F 2000 *Phys. Rev. Lett.* **85** 4076
Scopigno T, Balucani U, Ruocco G and Sette F 2000 *J. Phys.: Condens. Matter* **12** 8009
[63] Scopigno T, Balucani U, Ruocco G and Sette F 2002 *Phys. Rev.* E **65** 031205
[64] Li G, Du W M, Chen X K, Cummins H Z and Tao N J 1992 *Phys. Rev.* A **45** 3867
[65] Scopigno T, Ruocco G, Sette F and Viliani G 2002 *Phys. Rev.* E **66** 031205
[66] Bafile U, Verkerk P, Barocchi F, de Graaf L A, Suck J-B and Mutka H 1990 *Phys. Rev. Lett.* **65** 2394
[67] van Loef J J 1974 *Physica* **75** 115
[68] Bodensteiner T, Morkel Chr and Gläser W 1992 *Phys. Rev.* A **45** 5709
[69] Balucani U and Vallauri R 1990 *Chem. Phys. Lett.* **166** 77
[70] Frank F C 1952 *Proc. R. Soc.* A **215** 43
[71] Morkel Chr, Bodensteiner T and Gemperlein H 1993 *Phys. Rev.* E **47** 2575
[72] Noll F, Pilgrim W-C and Winter R 1988 *Z. Phys. Chem. N F* **156** 303

[73] Faber T E 1972 *Introduction to the Theory of Liquid Metals* (Cambridge: Cambridge University Press)
[74] Winter R and Hensel F 1989 *Phys. Chem. Liq.* **20** 1
[75] Winter R, Bodensteiner T, Gläser W and Hensel F 1987 *Ber. Bunsenges. Phys. Chem.* **95** 1133
[76] Freyland W 1979 *Phys. Rev.* B **20** 5104
[77] Franz G, Freyland W, Gläser W, Hensel F and Schneider E 1980 *J. Physique Coll.* **41** 194
[78] Matsuda K, Inui M, Kusakari M, Sakaguchi Y and Tamura K 2006 *J. Non-Cryst. Solids* at press
[79] Pasqualini D, Vallauri R, Demmel F, Morkel Chr and Balucani U 1999 *J. Non-Cryst. Solids* **250–252** 76
Demmel F, Diepold A and Morkel Chr 2000 *Physica* B **276–278** 456
[80] Balucani U, Torcini A and Vallauri R 1993 *Phys. Rev.* B **47** 3011
[81] Pilgrim W-C, Hosokawa S, Saggau H, Ross M and Yang L H 1999 *J. Non-Cryst. Solids* **250–252** 154
[82] de Gennes P G 1959 *Physica* **25** 825
[83] Hoshino K, Ugawa H and Watabe M 1992 *J. Phys. Soc. Japan* **61** 2182
[84] Jones R O and Gunnarson O 1989 *Rev. Mod. Phys.* **61** 689
[85] Pilgrim W-C, Ross M, Yang L and Hensel F 1997 *Phys. Rev. Lett.* **78** 3685
[86] Ross M, Yang L H, Dahling B and Winter N W 1994 *Z. Phys. Chem.* **184** 65
[87] Morse P M 1929 *Phys. Rev.* **34** 57
[88] Krauss M and Stevens W J 1990 *J. Chem. Phys.* **93** 4236
[89] Mao H K and Hemley R J 1994 *Rev. Mod. Phys.* **66** 671
[90] Reichlin R, Schiferl D, Martin S, Vanderborgh C and Mills R L 1985 *Phys. Rev. Lett.* **55** 1464
[91] Kahl G and Kambayashi S 1994 *J. Phys.: Condens. Matter* **6** 10897
[92] Bickham S R, Pfaffenzeller O, Collins L A, Kres J D and Hohl D 1998 *Phys. Rev.* B **58** R11813
[93] Schärpf O and Capellmann H 1993 *Phys. Status Solidi* a **135** 359
[94] Morkel C and Gläser W 1985 *Phys. Rev.* A **33** 3383
[95] Pilgrim W-C and Morkel C 2003 *Z. Phys. Chem.* **217** 957
[96] Sears V F 1984 *Thermal Neutron Scattering Length and Cross Sections for Condensed Matter Research* (Chalk River, ON: Chalk River Laboratories)
[97] Stangl A 1993 Single particle dynamics in liquid sodium *PhD Thesis* Technical University of Munich
[98] Balucani U, Torcini A, Stangl A and Morkel C 1995 *Phys. Scr.* T **57** 13
[99] Götze W and Zippelius A 1976 *Phys. Rev.* A **14** 1842
[100] Chapman S and Cowling T 1952 *The Mathematical Theory of Non-Uniform Gases* (Cambridge: Cambridge University Press)
[101] Erpenbeck J J and Alley W E 1984 *Phys. Today* **1** 56
[102] Erpenbeck J and Wood W 1991 *Phys. Rev.* A **43** 4254
[103] Hansen J P and McDonald J R 1976 *Theory of Simple Liquids* (London: Academic)
[104] Balucani U and Vallauri R 1990 *Nuovo Cimento* **12** 511
[105] Meyer R E and Nachtrieb N H 1955 *J. Chem. Phys.* **23** 1851
[106] Wahnström G and Sjögren L 1982 *J. Phys. C: Solid State Phys.* **15** 401
[107] de Schepper I M and Ernst H M 1979 *Physica* A **98** 189
[108] Pines D and Nozieres Ph 1966 *The Theory of Quantum Liquids* (New York: Benjamin)
[109] Bove L E, Dorner B, Petrillo C, Sacchetti F and Suck J-B 2003 *Phys. Rev.* B **68** 024208
[110] Bove L E, Sacchetti F, Petrillo C and Dorner B 2000 *Phys. Rev. Lett.* **85** 5352
[111] Bermejo F J *et al* 2000 *Phys. Rev. Lett.* **85** 106
[112] Delhommelle J and Petravic J 2003 *J. Chem. Phys.* **118** 2783
[113] Demmel F, Hosokawa S, Lorenzen M and Pilgrim W-C 2004 *Phys. Rev.* B **69** 012203
[114] Ernst M and Dorfman J 1975 *Stat. Phys.* **12** 311
[115] Pratesi G, Suck J-B and Egelstaff P A 1999 *J. Non-Cryst. Solids* **250–252** 91
[116] Boehler R and De Hantsetters K 2004 *High Pressure Res.* **24** 391